mathematics

Article

The Meshfree Radial Point Interpolation Method (RPIM) for Wave Propagation Dynamics in Non-Homogeneous Media

Cong Liu [1], Shaosong Min [1], Yandong Pang [2] and Yingbin Chai [3,4,*]

[1] College of Naval Architecture and Ocean Engineering, Naval University of Engineering, Wuhan 430033, China
[2] College of Weapon Engineering, Naval University of Engineering, Wuhan 430033, China
[3] School of Naval Architecture, Ocean and Energy Power Engineering, Wuhan University of Technology, Wuhan 430063, China
[4] State Key Laboratory of Ocean Engineering, Shanghai Jiao Tong University, Shanghai 200240, China
* Correspondence: chaiyb@whut.edu.cn

Abstract: This work presents a novel simulation approach to couple the meshfree radial point interpolation method (RPIM) with the implicit direct time integration method for the transient analysis of wave propagation dynamics in non-homogeneous media. In this approach, the RPIM is adopted for the discretization of the overall space domain, while the discretization of the time domain is completed by employing the efficient Bathe time stepping scheme. The dispersion analysis demonstrates that, in wave analysis, the amount of numerical dispersion error resulting from the discretization in the space domain can be suppressed at a very low level when the employed nodal support domain of the interpolation function is adequately large. Meanwhile, it is also mathematically shown that the amount of numerical error resulting from the time domain discretization is actually a monotonically decreasing function of the non-dimensional time domain discretization interval. Consequently, the present simulation approach is capable of effectively handling the transient analysis of wave propagation dynamics in non-homogeneous media, and the disparate waves with different speeds can be solved concurrently with very high computation accuracy. This numerical feature makes the present simulation approach more suitable for complicated wave analysis than the traditional finite element approach because the waves with disparate speeds always cannot be concurrently solved accurately. Several numerical tests are given to check the performance of the present simulation approach for the analysis of wave propagation dynamics in non-homogeneous media.

Keywords: meshfree techniques; numerical methods; spatial discretization; transient analysis; time integration

MSC: 35A08; 35A09; 35A24; 65L60; 74S05

check for updates

Citation: Liu, C.; Min, S.; Pang, Y.; Chai, Y. The Meshfree Radial Point Interpolation Method (RPIM) for Wave Propagation Dynamics in Non-Homogeneous Media. *Mathematics* **2023**, *11*, 523. https://doi.org/10.3390/math11030523

Academic Editors: Zhuojia Fu, Yiqian He and Hui Zheng

Received: 9 December 2022
Revised: 15 January 2023
Accepted: 16 January 2023
Published: 18 January 2023

1. Introduction

In many engineering application areas, transient wave propagation dynamics are frequently encountered [1,2]. In essence, solving this type of engineering problem is to effectively handle the time-continuous governing partial differential equations via numerical approaches. In practice, the finite element approach with the direct time integration algorithm is widely utilized to solve complex transient wave propagation dynamics [3]. The finite element method (FEM) is mainly adopted to achieve the discretization of the overall space domain. Then, a series of semi-discrete dynamic equations, which are discrete in the space domain and continuous in the time domain, can be obtained. By using the appropriate time integration algorithms, the required discretization in the time domain can also be realized, and then the considered transient wave propagations can finally be solved.

Although a large number of spatial discretization schemes can be exploited to discretize the involved problem domain spatially (such as the finite difference method [4–7], the spectral element method [8], the smoothed FEM [9–19], the meshless techniques [20–29], and the boundary element or boundary-based numerical algorithms [30–41]), the traditional finite element approach is still dominantly employed in practice due to its relatively firm mathematical background and easy implementation. Nevertheless, the finite element approach also suffers from several inherent shortcomings in wave analysis [1,3,42]. One intractable issue of them is that the concomitant spatial discretization error always arises in the numerical solutions and cannot be completely avoided [42]. Actually, the resultant spatial discretization error is closely related to the number of employed elements per wavelength. More elements in one wavelength can lead to a smaller amount of discretization error. In engineering practice, only the relatively low vibration modes can be accurately represented when a fixed mesh pattern is used. For the relatively high-vibration modes, the obtained spatial discretization error is usually quite large because they are not spatially resolved with sufficiently high accuracy. In solving the transient wave propagation dynamics, these spatial discretization errors in high-order vibration modes will pollute the obtained numerical solutions and can give rise to many spurious oscillations [3].

Compared to the conventional finite element approach, meshless numerical techniques might be a powerful alternative to enhance the performance of traditional FEM in spatial discretization for wave analysis [20]. In the meshless framework, only a set of scattered field nodes are used to represent the involved physical space domain, and the pre-defined meshes or elements are not required [20]. In consequence, the computed numerical solutions from the meshless techniques are usually insensitive to the employed node distribution schemes, while this factor can severely affect the solution quality of the traditional FEM because the distorted meshes can lead to very inaccurate solutions. Additionally, the higher-order numerical approximation can always be achieved by meshless techniques, and then in wave analysis, the possible spatial discretization errors can be largely suppressed. Consequently, the high-order vibration modes also can be well represented, and the spurious oscillations in the solutions can be effectively eliminated. During the past few decades, various meshfree numerical techniques have been developed and used in a large range of engineering and scientific computation fields, such as the smoothed particle hydrodynamics (SPH) [43], the reproducing kernel particle method (RKPM) [44], the element-free Galerkin method (EFGM) [45–47], the method of finite spheres (MFS) [48] and various strong-form collocation methods [49–53]. Due to the relatively high numerical performance of the RPIM in a large number of numerical tests and the possession of the Kronecker delta function property [20], the meshless RPIM is utilized in this work to achieve the required spatial discretization in transient wave analysis.

In addition to spatial discretization, discretization in the time domain is also an indispensable step to handle complex time-continuous dynamic equations. The widely used numerical treatment for this step is to use a direct time integration algorithm. In the direct time integration schemes, the required discretization in the time domain can be achieved without any additional numerical treatments on the obtained system mass and stiffness matrices. Generally, the frequently used direct time integration algorithms in practice can be classified into two types, namely the explicit direct time integration algorithm [54,55] and the implicit direct time integration algorithm [56,57]. In the explicit time integration algorithm, only the information of the field function variables (such as displacements, velocities, and accelerated velocities) at the previous time point is needed to calculate the response at the current time point. The treatment of the simultaneous equations can be easily avoided in an explicit time integration algorithm. However, the explicit time integration algorithm is always conditionally stable. Consequently, there always exists a critical time step increment in the numerical integration process. Due to this issue, stable and reliable numerical solutions can be yielded unless the employed time step for time integration is not larger than the critical time step increment.

In contrast to the explicit time integration algorithm, in the implicit time integration scheme, both the variable information at the previous and current time points are required to compute the responses at the current time point. In general, the treatment of the simultaneous equations cannot be avoided in an implicit method. However, the implicit direct time integration algorithm is always unconditionally stable, and there exists no so-called critical time step increment. As a result, a relatively large time integration step can be used for a stable numerical solution, and then the required number of time steps can be largely reduced. Similar to the discretization in the space domain, the discretization in the time domain can also give rise to considerable numerical errors. In general, the numerical errors induced by temporal discretization are mainly determined by the order of the computational accuracy and the temporal discretization step used.

In this work, the two-step implicit Bathe time integration algorithm is employed to complete the discretization in the time domain due to the fact that excellent numerical features can be obtained in solving complex linear and nonlinear structural dynamics [58]. It should be noted that the numerical spatial discretization error induced by the RPIM can be suppressed at a very low level; hence, it is reasonable to expect that the RPIM with the Bathe time integration algorithm might be a powerful numerical approach to solve the transient wave propagation dynamic problems. Actually, this novel simulation approach has been developed to handle the transient wave propagations in homogeneous media [59]. It has been demonstrated by the numerical tests and dispersion analysis that quite fine numerical solutions can be yielded. More importantly, it is very interesting to find that the so-called monotonic convergence property can be basically reached by this numerical approach in transient wave analysis; namely, the quality of the obtained numerical solutions will be better when the non-dimensional temporal discretization step used gets smaller. Due to this good and valuable numerical feature, this numerical approach is particularly suitable for the analysis of complicated transient wave propagation problems, such as wave propagation in non-homogeneous media and composite structures. The contents of this work are mainly motivated by this idea, and the potential powerful ability of this simulation approach in solving the transient wave propagations in non-homogeneous media is investigated in great detail in this work.

2. Problem Statement

We consider the involved wave propagation domain contains two different regions, Ω_1 and Ω_2, with the interface Γ (See Figure 1). Suppose that the different regions are occupied with different acoustic fluid media. When the considered acoustic fluid media are inviscid and compressible, for the linear theory of acoustics, the acoustic pressure p is governed by the following equations:

$$\begin{cases} \nabla^2 p_1 - \frac{1}{c_1^2}\frac{\partial^2 p_1}{\partial t^2} = 0, \text{ in } \Omega_1 \\ \nabla^2 p_2 - \frac{1}{c_2^2}\frac{\partial^2 p_2}{\partial t^2} = 0, \text{ in } \Omega_2 \end{cases}, \tag{1}$$

in which ∇^2 represents the Laplace operator, p_i (i = 1,2) are the acoustic pressures in different acoustic fluid regions, c_i (i = 1,2) are the corresponding acoustic wave speeds, and t denotes the time variable.

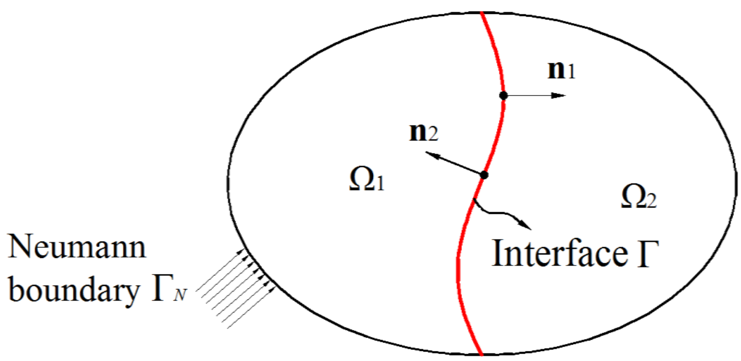

Figure 1. The involved wave propagation domain in which non-homogeneous media are considered.

On the interface of the different wave propagation regions, the following continuity conditions of acoustic pressure and normal acoustic particle velocity should be satisfied:

$$\begin{cases} p_1 = p_2 \\ \frac{1}{\rho_1}\nabla p_1 \cdot \mathbf{n}_1 + \frac{1}{\rho_2}\nabla p_2 \cdot \mathbf{n}_2 = 0 \end{cases}, \text{ on } \Gamma, \tag{2}$$

in which ρ_i ($i = 1,2$) are the mass densities of the considered acoustic fluid media in different regions, and $\mathbf{n}_i$ ($i = 1,2$) stand for the outward normal unit vector on interface Γ.

According to the principle of virtual work, the governing equations of acoustic wave propagation in non-homogeneous media can be written in the following integral form [1,60–62]:

$$\sum_{i=1}^{2} \int_{\Omega_i} \overline{p}(\nabla^2 p_i - \frac{1}{c_i^2}\frac{\partial^2 p_i}{\partial t^2}) d\Omega = 0, \tag{3}$$

in which $\overline{p}$ denotes the assumed "virtual" acoustic pressure distributions.

It should be noted that $\overline{p}$ in Equation (3) is arbitrary, hence the satisfaction of Equation (3) requires that the field variables in the bracket should be zero. Therefore, Equation (3) is actually equivalent to the original governing equation in Equation (1).

In order to decrease the order of derivatives in Equation (3), by using the divergence theorem, the following equation can be obtained:

$$\sum_{i=1}^{2} \left(\int_{\Omega_i} \nabla\overline{p} \cdot \nabla p_i \mathrm{d}\Omega + \frac{1}{c_i^2}\int_{\Omega_i} \overline{p}\frac{\partial^2 p_i}{\partial t^2}\mathrm{d}\Omega - \int_{\Gamma_N} \overline{p}(\nabla p_i \cdot \mathbf{n}_i)\mathrm{d}\Gamma \right) = 0, \tag{4}$$

in which Γ_N denotes the involved Neumann boundary conditions (see Figure 1).

In this work, the Lagrange multipliers are employed to handle the acoustic wave propagation in non-homogeneous media in which the discontinuities in the gradient fields of acoustic pressure are usually involved in the interface of different acoustic fluid media. By using the usual field function approximation in the standard finite element approach and the well-known Lagrange multiplier technique, the following equations in matrix form can be obtained from Equation (4):

$$\begin{cases} \frac{1}{c_1^2}\int_{\Omega_1} \mathbf{N}_{f_1}^T \mathbf{N}_{f_1} \frac{\partial^2 \mathbf{p}_1}{\partial t^2}\mathrm{d}\Omega + \int_{\Omega_1} \left(\nabla \mathbf{N}_{f_1}\right)^T \nabla \mathbf{N}_{f_1}\mathbf{p}_1 \mathrm{d}\Omega - \int_{\Gamma_N} \mathbf{N}_{f_1}^T(\nabla p_1 \cdot \mathbf{n}_1)\mathrm{d}\Gamma \\ -\int_{\Gamma} \left(\nabla \mathbf{N}_{f_1}\right)^T \mathbf{n}_1 \mathbf{N}_\lambda \frac{1}{\rho_1}\boldsymbol{\lambda}\mathrm{d}\Gamma = \mathbf{0} \\ \frac{1}{c_2^2}\int_{\Omega_2} \mathbf{N}_{f_2}^T \mathbf{N}_{f_2} \frac{\partial^2 \mathbf{p}_2}{\partial t^2}\mathrm{d}\Omega + \int_{\Omega_2} \left(\nabla \mathbf{N}_{f_2}\right)^T \nabla \mathbf{N}_{f_2}\mathbf{p}_2 \mathrm{d}\Omega - \int_{\Gamma_N} \mathbf{N}_{f_2}^T(\nabla p_2 \cdot \mathbf{n}_2)\mathrm{d}\Gamma \\ -\int_{\Gamma} \left(\nabla \mathbf{N}_{f_2}\right)^T \mathbf{n}_2 \mathbf{N}_\lambda \frac{1}{\rho_2}\boldsymbol{\lambda}\mathrm{d}\Gamma = \mathbf{0} \\ -\int_{\Gamma} \mathbf{N}_\lambda^T \mathbf{n}_1 \left(\nabla \mathbf{N}_{f_1}\right) \frac{1}{\rho_1}\mathbf{p}_1 \mathrm{d}\Gamma - \int_{\Gamma} \mathbf{N}_\lambda^T \mathbf{n}_2 \left(\nabla \mathbf{N}_{f_2}\right) \frac{1}{\rho_2}\mathbf{p}_2 \mathrm{d}\Gamma = \mathbf{0} \end{cases}, \tag{5}$$

in which $\mathbf{N}_{f_1}$ and $\mathbf{N}_{f_2}$ represent the constructed nodal interpolation functions for the acoustic pressure in different regions, and $\mathbf{N}_\lambda$ is the nodal interpolation function for the Lagrange multiplier $\boldsymbol{\lambda}$ on the interface Γ.

Of course, Equation (5) can also be expressed in the following simplified form:

$$\begin{bmatrix} \mathbf{M}_1 & \mathbf{0} & \mathbf{0} \\ \mathbf{0} & \mathbf{M}_2 & \mathbf{0} \\ \mathbf{0} & \mathbf{0} & \mathbf{0} \end{bmatrix} \begin{bmatrix} \ddot{\mathbf{p}}_1 \\ \ddot{\mathbf{p}}_2 \\ \ddot{\boldsymbol{\lambda}} \end{bmatrix} + \begin{bmatrix} \mathbf{K}_1 & \mathbf{0} & \mathbf{A} \\ \mathbf{0} & \mathbf{K}_2 & \mathbf{G} \\ \mathbf{A}^T & \mathbf{G}^T & \mathbf{0} \end{bmatrix} \begin{bmatrix} \mathbf{p}_1 \\ \mathbf{p}_2 \\ \boldsymbol{\lambda} \end{bmatrix} = \begin{bmatrix} \mathbf{R}_1 \\ \mathbf{R}_2 \\ \mathbf{0} \end{bmatrix}, \tag{6}$$

in which

$$\begin{array}{l}
\mathbf{M}_1 = \frac{1}{c_1^2}\int_{\Omega_1} \mathbf{N}_{f_1}^T \mathbf{N}_{f_1} \mathrm{d}\Omega, \;\; \mathbf{M}_2 = \frac{1}{c_2^2}\int_{\Omega_2} \mathbf{N}_{f_2}^T \mathbf{N}_{f_2} \mathrm{d}\Omega \\
\mathbf{K}_1 = \int_{\Omega_1} \left(\nabla \mathbf{N}_{f_1}\right)^T \nabla \mathbf{N}_{f_1} \mathrm{d}\Omega, \;\; \mathbf{K}_2 = \int_{\Omega_2} \left(\nabla \mathbf{N}_{f_2}\right)^T \nabla \mathbf{N}_{f_2} \mathrm{d}\Omega \\
\mathbf{A} = -\int_{\Gamma} \left(\nabla \mathbf{N}_{f_1}\right)^T \mathbf{n}_1 \mathbf{N}_{\lambda} \frac{1}{\rho_1} \mathrm{d}\Gamma, \;\; \mathbf{G} = -\int_{\Gamma} \left(\nabla \mathbf{N}_{f_2}\right)^T \mathbf{n}_2 \mathbf{N}_{\lambda} \frac{1}{\rho_2} \mathrm{d}\Gamma \\
\mathbf{R}_1 = \int_{\Gamma_N} \mathbf{N}_{f_1}^T (\nabla p_1 \cdot \mathbf{n}_1) \mathrm{d}\Gamma, \;\; \mathbf{R}_2 = \int_{\Gamma_N} \mathbf{N}_{f_2}^T (\nabla p_2 \cdot \mathbf{n}_2) \mathrm{d}\Gamma
\end{array}, \tag{7}$$

3. A Brief Review of the Meshfree RPIM

In the meshfree RPIM framework, the constructed numerical approximation for the considered field function is obtained by using a series of scattered field points in the problem domain (see Figure 2). In addition, the numerical approximation is also enforced to pass through the function values at the involved field points. In the classical and well-developed RPIM, the radial basis functions (RBFs) are combined with the frequently used polynomial basis functions (PBFs) to create the required numerical approximation.

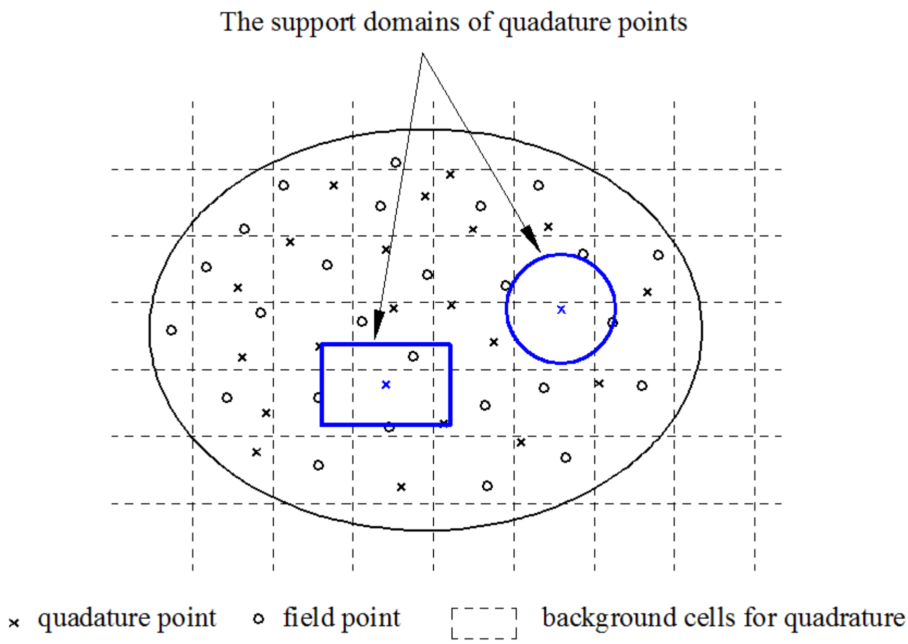

Figure 2. The description of constructed numerical approximation for the considered field function using the typical meshfree RPIM.

For an involved problem domain that is represented by a series of field nodes, suppose that a scalar function $u(\mathbf{x})$ is defined on it, and the corresponding field function approximation using RPIM for $u(\mathbf{x})$ can be expressed by [20]

$$u_h(\mathbf{x}) = \sum_{i=1}^{n} R_i(\mathbf{x}) a_i + \sum_{j=1}^{m} p_j(\mathbf{x}) b_j = \mathbf{R}^T(\mathbf{x})\mathbf{a} + \mathbf{p}^T(\mathbf{x})\mathbf{b}, \tag{8}$$

in which $R_i(\mathbf{x})$ is the employed RBF in creating the numerical approximation for node i, and a_i is the corresponding interpolation coefficient; $p_j(\mathbf{x})$ is the employed PBF, and b_j is the corresponding interpolation coefficient; and n and m are the numbers of the employed RBFs and PBFs, respectively.

In this work, we only use the linear PBF. For the numerical approximation in two-dimensional space, m = 3. On the contrary, the number of the used RBF for numerical approximation is determined by the size of the employed local support domain. In general, the vector of RBF in Equation (8) can be written by

$$\mathbf{R}^T(\mathbf{x}) = \begin{bmatrix} R_1(\mathbf{x}) & R_2(\mathbf{x}) & R_3(\mathbf{x}) & \cdots & R_n(\mathbf{x}) \end{bmatrix}, \tag{9}$$

In practice, the required RBF can be constructed in different ways, and different types of RBF usually have different numerical features [20,63]. In this work, the classical multi-quadric (MQ) basis, which is frequently used in surface fitting, is employed to construct the RBF. The explicit expression of MQ is given by

$$R_i(\mathbf{x}) = \left[r_i^2 + (\alpha_c d_c)^2 \right]^q, \tag{10}$$

in which r_i is the distance from the field node $\mathbf{x}_i$ to the interest point $\mathbf{x}$, d_c is the defined characteristic length of the used field node distribution pattern, and α_c and q are two related parameters to control the shape of the MQ. Here, $q = 1.03$ and $\alpha_c = 1$ are directly used due to the fact that very good numerical performance can be obtained with these parameters by a large number of numerical experiments in computational solid and fluid mechanics [20,64,65].

For the linear PBF in Equation (8), the vector of PBF is

$$\begin{cases} \mathbf{p}^T(\mathbf{x}) = \begin{bmatrix} 1 & x \end{bmatrix}, & \text{for 1D space} \\ \mathbf{p}^T(\mathbf{x}) = \begin{bmatrix} 1 & x & y \end{bmatrix}, & \text{for 2D space}, \\ \mathbf{p}^T(\mathbf{x}) = \begin{bmatrix} 1 & x & y & z \end{bmatrix}, & \text{for 3D space} \end{cases} \tag{11}$$

Suppose that the numerical approximation in Equation (8) is satisfied at n involved field nodes in the local support domain, namely

$$u_i(\mathbf{x}) = \sum_{i=1}^{n} R_i(\mathbf{x}) a_i + \sum_{j=1}^{m} p_j(\mathbf{x}) b_j, \; i = 1, 2, \cdots, n, \tag{12}$$

In order to make the interpolation coefficients a_i and b_j unique, the following constraints are also required:

$$\sum_{i=1}^{n} p_j(\mathbf{x}_i) a_i = 0, \; j = 1, 2, \cdots, m, \tag{13}$$

By combining Equations (12) and (13), we can have

$$\begin{bmatrix} \mathbf{u} \\ \mathbf{0} \end{bmatrix} = \underbrace{\begin{bmatrix} \mathbf{R}_Q & \mathbf{P}_m \\ \mathbf{P}_m^T & \mathbf{0} \end{bmatrix}}_{\mathbf{G}} \underbrace{\begin{bmatrix} \mathbf{a} \\ \mathbf{b} \end{bmatrix}}_{\mathbf{a}_0} = \mathbf{G}\mathbf{a}_0, \tag{14}$$

in which

$$\mathbf{R}_Q = \begin{bmatrix} R_1(r_1) & R_2(r_1) & \cdots & R_n(r_1) \\ R_1(r_2) & R_2(r_2) & \cdots & R_n(r_2) \\ \vdots & \vdots & \ddots & \vdots \\ R_1(r_n) & R_2(r_n) & \cdots & R_n(r_n) \end{bmatrix}_{n \times n}, \tag{15}$$

$$\mathbf{P}_m = \begin{bmatrix} P_1(\mathbf{x}_1) & P_2(\mathbf{x}_1) & \cdots & P_m(\mathbf{x}_1) \\ P_1(\mathbf{x}_2) & P_2(\mathbf{x}_2) & \cdots & P_m(\mathbf{x}_2) \\ \vdots & \vdots & \ddots & \vdots \\ P_1(\mathbf{x}_n) & P_2(\mathbf{x}_n) & \cdots & P_m(\mathbf{x}_n) \end{bmatrix}_{n \times m}, \tag{16}$$

$$\mathbf{a}_0^T = \begin{bmatrix} a_1 & a_2 & \cdots & a_n & b_1 & b_2 & \cdots & b_m \end{bmatrix}, \tag{17}$$

Following the standard formulation of the RPIM, the following matrix equation can be obtained [20,64]:

$$\begin{cases} u_h(\mathbf{x}) = \mathbf{R}^T(\mathbf{x})\mathbf{a} + \mathbf{p}^T(\mathbf{x})\mathbf{b} = \left[\mathbf{R}^T(\mathbf{x})\mathbf{S}_a + \mathbf{p}^T(\mathbf{x})\mathbf{S}_b\right]\mathbf{u}_s = \mathbf{\Phi}(\mathbf{x})\mathbf{u} \\ \mathbf{S}_a = \left(\mathbf{R}_Q^{-1} - \mathbf{R}_Q^{-1}\mathbf{P}_m\mathbf{S}_b\right) \\ \mathbf{S}_b = \left[\mathbf{P}_m^T\mathbf{R}_Q^{-1}\mathbf{P}_m\right]\mathbf{P}_m^T\mathbf{R}_Q^{-1} \end{cases}, \tag{18}$$

in which $\mathbf{\Phi}(\mathbf{x})$ is the constructed nodal interpolation function matrix in the classical RPIM framework.

4. Numerical Error Evaluation in Transient Wave Analysis

In engineering practice, the governing equation for transient wave propagation is continuous both in the space and time domains. To effectively handle this problem by means of the numerical approaches, both the discretization schemes in the space and time domains are needed. Unfortunately, not only the discretization in the space domain but also the discretization in the time domain are able to cause a considerable amount of numerical errors in the computed numerical solutions. In this section, the resultant numerical errors in transient wave analysis will be systemically investigated. Owing to the excellent numerical properties which have been demonstrated in previously published papers [20,64,65], the classical meshfree RPIM and the two-stage time stepping Bathe method are respectively responsible for the required discretization in space and time domain.

For the linear theory of acoustics, the governing equation of transient acoustic wave propagation in an ideal acoustic fluid can be easily obtained by

$$\nabla^2 p - \frac{1}{c^2}\frac{\partial^2 p}{\partial t^2} = 0, \tag{19}$$

As usual, when the considered acoustic pressure variable p is time-harmonic, the following reduced governing equation for wave propagation can be obtained from Equation (19):

$$\nabla^2 P + k^2 P = 0, \tag{20}$$

in which P is the spatial distribution of acoustic pressure, and k stands for the wave number.

It should be noted that Equation (20) is actually the well-known Helmholtz equation in state steady wave analysis, and it is clear that Equation (20) is time-independent. To solve Equation (20) numerically, only the related discretization in the space domain is required. Here, we first investigate the numerical error properties when different spatial discretization techniques are exploited to handle Equation (20). The evenly placed node distribution shown in Figure 3 is employed for numerical error evaluation in this section.

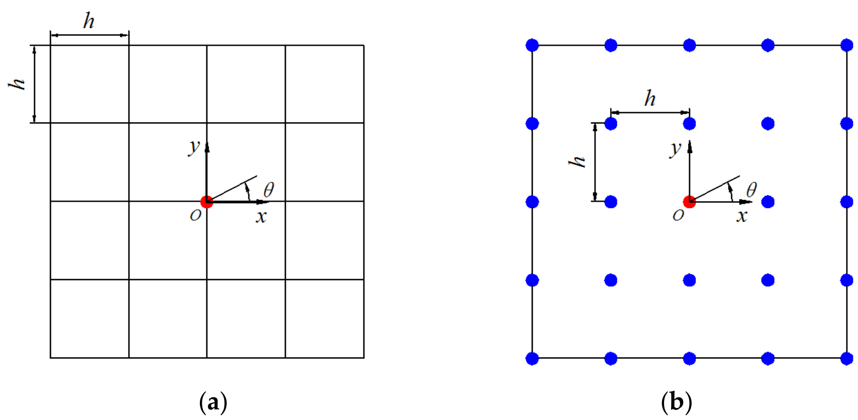

Figure 3. The evenly placed node distributions for numerical error evaluation using different numerical approaches: (**a**) FEM-Q4; (**b**) RPIM.

Using the classical Galerkin weighted residual numerical techniques, the following matrix equation can be obtained from Equation (20) [60,66–69]:

$$\mathbf{KP} - k^2\mathbf{MP} = \mathbf{0}, \tag{21}$$

in which $\mathbf{P}$ is the nodal unknowns for the acoustic pressure, and $\mathbf{K}$ and $\mathbf{M}$ are the resultant matrices corresponding to the system stiffness and mass, respectively [60].

It is clear that Equation (21) has the following fundamental numerical solutions:

$$\mathbf{P} = \mathbf{A}e^{jk_h\mathbf{x}\cdot\mathbf{n}}, \tag{22}$$

In which $\mathbf{x}$ is a position vector of the point of interest, $\mathbf{A}$ is the amplitude of the acoustic pressure distribution vector, and k_h denotes the wave number of numerical solutions.

Since no boundary conditions are involved here, the amplitude of acoustic pressure distribution for all nodes should hence be identical.

Taking Equation (22) into Equation (21), the following characteristic equation can be arrived at [60]:

$$\left(D_{\text{stiffness}} - k^2 D_{\text{mass}}\right)\mathbf{A} = \mathbf{0}, \tag{23}$$

in which $D_{\text{stiffness}}$ and D_{mass} are two characteristic parameters that are closely related to the system stiffness and mass, respectively. $D_{\text{stiffness}}$ and D_{mass} can be directly computed using the related formulations in Refs. [60,66].

For the non-trivial solutions of Equation (23), we have

$$k = \sqrt{\frac{D_{\text{stiffness}}}{D_{\text{mass}}}}, \tag{24}$$

From Refs. [60,66], it is known that both $D_{\text{stiffness}}$ and D_{mass} are functions of the numerical wave number k_h. Therefore, the relationship between the exact wave number k and the numerical wave number k_h can be successfully built via Equation (24).

In this work, the following error indicator is employed to perform the numerical error evaluation from the discretization in space domain:

$$\varepsilon = \frac{k}{k_h}. \tag{25}$$

To compare the numerical performance of the different spatial discretization schemes in tackling the Helmholtz equation, the meshfree RPIM with different support domain sizes of the quadrature points and the traditional bilinear quadrilateral elements (FEM-Q4) are mainly considered in this work. For simplicity, in all numerical experiments, the standard four-node quadrilateral mesh patterns for the FEM-Q4 are directly employed as the background numerical integration cells for the RPIM.

Figure 4 compares the numerical spatial discretization error results along different angles of wave travel ($\theta = 0°$, $\theta = 15°$, $\theta = 30°$, and $\theta = 45°$) as the functions of the non-dimensional wave numbers $k_h h$ (h stands for the characteristic length of the nodal space) from the above-mentioned spatial discretization methods. Looking at Figure 4d, it is apparent that the calculated numerical errors from the FEM-Q4 grow quickly when the considered non-dimensional wave numbers get larger. This means that the traditional FEM-Q4 is not able to behave sufficiently well in suppressing the numerical errors from the discretization in the space domain. Figure 4 also displays the computed numerical errors from the RPIM when different support domain sizes ($\alpha_s = h$, $\alpha_s = 2h$, and $\alpha_s = 3h$) of quadrature points are employed; here, α_s stands for the characteristic length of the employed local square support domain.

The numerical results in Figure 4 illustrate that the RPIM is able to produce much smaller numerical errors than the conventional FEM-Q4.This is because the high-order numerical approximation can be reached in formulating the RPIM. In addition, one clear trend can also be observed from Figure 4 that the abilities of the RPIM in suppressing the numerical will become stronger when the used local support domain size gets larger. In particular, the computed numerical errors along all angles are very close to zero when the local support domain size $\alpha_s = 3h$. Due to this observation, in the following numerical tests, we only consider the local support domain size $\alpha_s = 3h$.

As stated in previous texts, in addition to the discretization in the space domain, the discretization in the time domain also can lead to numerical errors in transient wave analysis. From the related research in Ref. [60], it is known that the total numerical errors (both the numerical errors from the spatial and temporal discretizations are contained) can be explicitly expressed by the following equation:

$$\frac{c_h}{c} = \frac{k}{k_h}\frac{T}{T_h}, \tag{26}$$

in which c is the acoustic wave speed, and T represents the period of the considered wave mode; the subscript "h" means that the corresponding field variables are from the numerical solutions.

In the right hand of Equation (26), the first term k/k_h stands for the numerical errors from the discretization in the space domain, and the second term T/T_h is mainly caused by the temporal discretization. In this work, the Bathe method, which is a typical two-stage time-stepping implicit temporal discretization numerical technique [1], is employed for the required temporal discretization. It has been demonstrated mathematically that the temporal discretization errors T/T_h from the Bathe method are actually a monotonically decreasing function of the non-dimensional temporal discretization interval CFL [60] (CFL = $c\Delta t/h$, Δt is the time increment for time integration). When the used CFL trends to zero, the resultant temporal discretization error will also trend to zero, i.e., $T/T_h \to 1$. With this numerical property, the total numerical error in transient wave analysis can also be roughly regarded as a monotonically decreasing function of the non-dimensional temporal discretization interval CFL when the numerical errors from the discretization in the space domain are sufficiently small (in particular, $k/k_h \to 1$ is required).

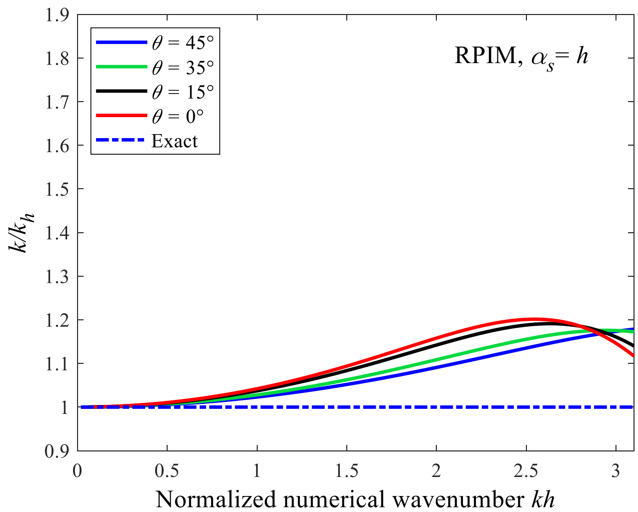

(**a**)

Figure 4. *Cont.*

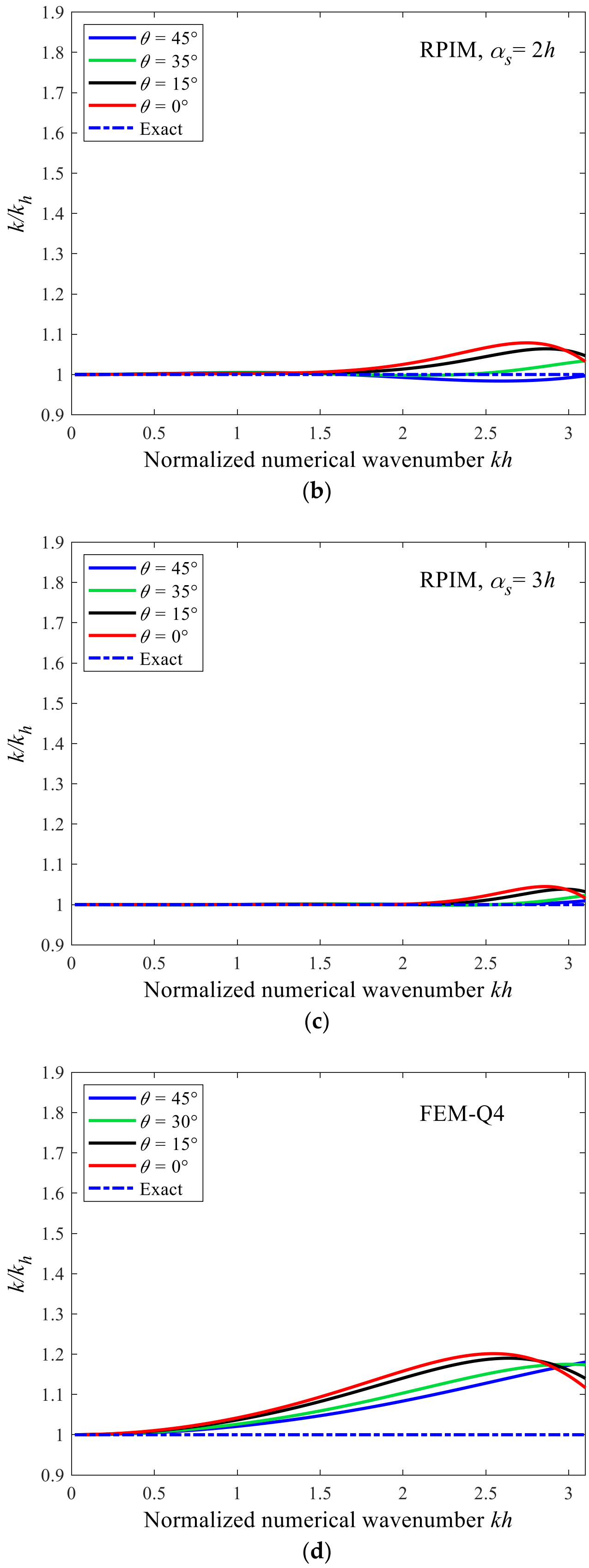

Figure 4. Comparisons of the numerical spatial discretization error results along different angles of wave travel as the functions of the non-dimensional wave numbers from disparate spatial discretization methods: (**a**) RPIM with $\alpha_s = h$; (**b**) RPIM with $\alpha_s = 2h$; (**c**) RPIM with $\alpha_s = 3h$; (**d**) FEM-Q4.

From the previous analysis and discussion, it is clearly displayed that the meshfree RPIM is able to generate close-to-zero spatial discretization errors when the employed local support domain size $\alpha_s = 3h$. Therefore, it is very reasonable to expect that the computed numerical solutions can become more accurate when the employed temporal discretization interval CFL becomes smaller. In other words, the present meshfree RPIM with the Bathe method has the so-called monotonic convergence property in handling the transient wave propagation dynamics [59,60]. However, the traditional numerical approach in transient wave analysis does not have this interesting and important numerical feature. Due to this good numerical feature, the wave propagation property of different wave components at different wave speeds can be simulated very accurately. Therefore, the numerical approach presented in this work is particularly suitable for solving very complex wave propagations. In the next section, the numerical feature of the present approach will be examined carefully by solving three typical numerical experiments in which the transient wave propagations in non-homogeneous media are considered.

5. Numerical Results

5.1. One Two-Dimensional Tube Filled with Different Media

As shown in Figure 5, one two-dimensional tube, which is filled with two different types of acoustic fluid media, is first considered here. This two-dimensional tube has a length of L = 1 m and a width of b = 0.1 m. The left and right halves of this tube are filled with different media with fluid density ρ and acoustic wave speed c. The related material constants are $\rho_1 = \rho_2$, c_1 = 1 m/s, and c_2 = 0.5 m/s. The required spatial discretization of the involved problem domain for this numerical example is first achieved by using the evenly placed node distributions with the nodal interval h = 0.0125 m. The corresponding spatial discretization patterns for different methods are given in Figure 6. Suppose that a sinusoidal acoustic wave, $p = \sin 16\pi t$ Pa with $t \in [0, 0.0625]$s, is traveling along this tube from the left end. In this numerical example, the non-dimensional time integration step size used is measured by CFL = $c_1 \Delta t/h$.

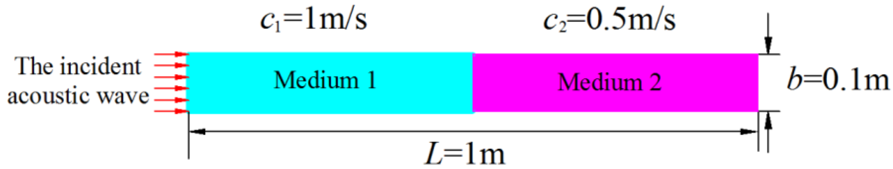

Figure 5. The transient wave propagation in a two-dimensional tube filled with different media.

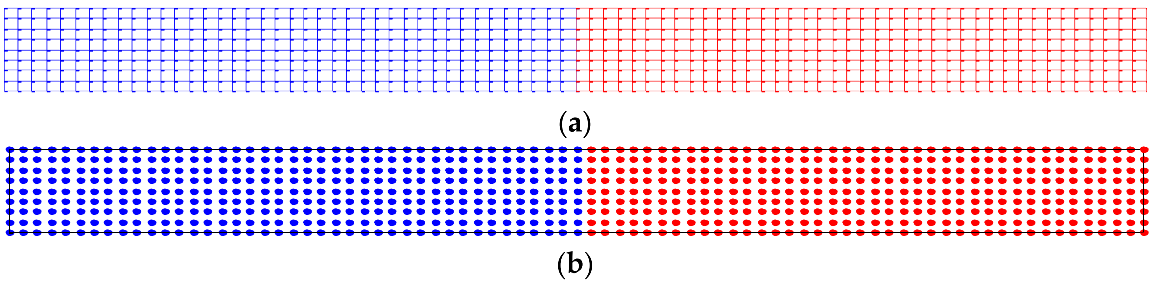

Figure 6. The used spatial discretization of the two-dimensional tube for different methods: (**a**) FEM-Q4; (**b**) RPIM.

Figure 7 compares the computed numerical solutions of the acoustic pressure distributions from the standard FEM-Q4 and the present meshfree RPIM with the identical node distribution schemes (see Figure 6) when the considered time point t = 0.4 s and the employed non-dimensional time integration step size CFL = 0.1. With the aim to compare the numerical performance of different numerical approaches in terms of computation accuracy, the exact solutions are also provided in the figures here. One important finding from Figure 7 is that the FEM-Q4 solutions are not sufficiently accurate because the obvious spurious oscillations can be clearly seen behind the wave front. In contrast to the FEM-Q4 solutions, the present meshfree RPIM is able to generate much more accurate solutions which are quite consistent with the exact solutions. Additionally, when the time point t = 0.8 s, the corresponding numerical solutions of acoustic pressure distributions from different numerical approaches are also computed and displayed in Figure 8. In this situation, both the reflected and transmitted acoustic waves can be induced by the interface of the two different fluid media. Figure 8 indicates that the outcome for this case is quite similar to that when the time point t = 0.4 s because the FEM-Q4 solutions exhibit clear spurious oscillations in both the reflected and transmitted acoustic waves, while the meshfree RPIM solutions are very close to the exact solutions and the resultant spurious oscillations are much smaller compared to those from the FEM-Q4 solutions. A possible explanation for these observations might be that the present meshfree RPIM is able to yield much smaller numerical dispersion errors from spatial discretization than the standard FEM-Q4, which has been reported in Figure 4.

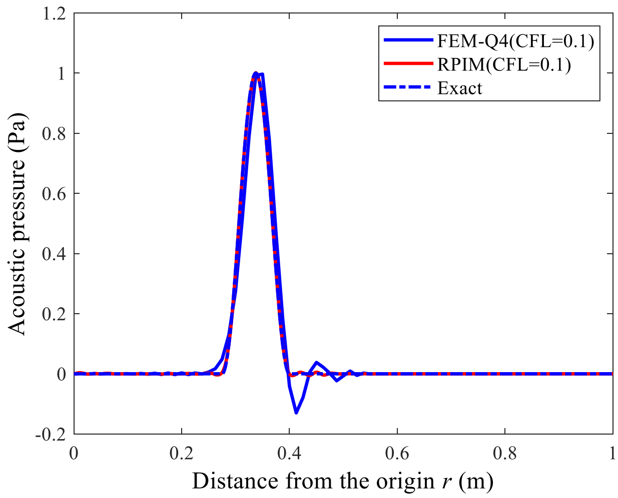

Figure 7. The computed numerical solutions of the acoustic pressure distributions for the two-dimensional tube from different numerical approaches when the time point t = 0.4 s.

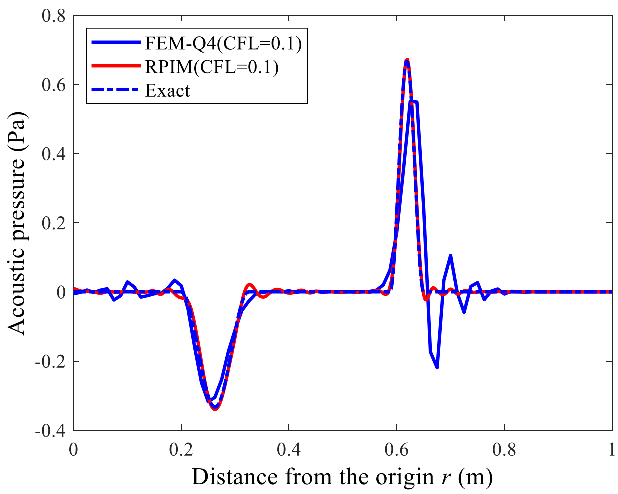

Figure 8. The computed numerical solutions of the acoustic pressure distributions for the two-dimensional tube from different numerical approaches when the time point t = 0.8 s.

Additionally, the acoustic pressure distribution results from different numerical approaches are also computed when the varying non-dimensional time integration steps are employed (CFL = 1, CFL = 0.5, CFL = 0.25, and CFL = 0.1). For the time points t = 0.4 s and t = 0.8 s, the corresponding numerical solutions are displayed in Figures 9 and 10, respectively. The results in these figures show that the quality of the numerical results from the standard FEM-Q4 does not become better when the smaller non-dimensional time integration step is used. In particular, more unwanted spurious oscillations can be observed in the FEM-Q4 solutions when the non-dimensional time integration step CFL = 0.1. In contrast to the observations which can be seen in the FEM-Q4 solutions, it is quite surprising that the present meshfree RPIM is able to generate more accurate and reliable acoustic pressure distribution results when we use smaller non-dimensional time integration steps. Therefore, we can reach one important conclusion that in transient wave analysis, the present meshfree RPIM with the Bathe temporal discretization scheme possesses the ability to achieve better numerical solutions by decreasing the employed non-dimensional time integration steps, namely the so-called monotonic convergence property in transient wave analysis can be broadly reached. Owing to this valuable numerical feature, the present meshfree RPIM is able to stand out clearly from the existing conventional numerical approaches in transient wave analysis. The above findings from Figures 9 and 10 may be explained by the fact that the present meshfree RPIM is able to generate almost no dispersion errors, which is related to the discretization in the space domain, while the corresponding dispersion errors from FEM-Q4 are relatively large. Meanwhile, the additional numerical errors from the Bathe temporal discretization scheme are actually a monotonically decreasing function of the employed non-dimensional time integration step. As a result, the monotonic convergence property in transient wave analysis can be broadly reached by the meshfree RPIM and cannot be reached by the traditional FEM-Q4.

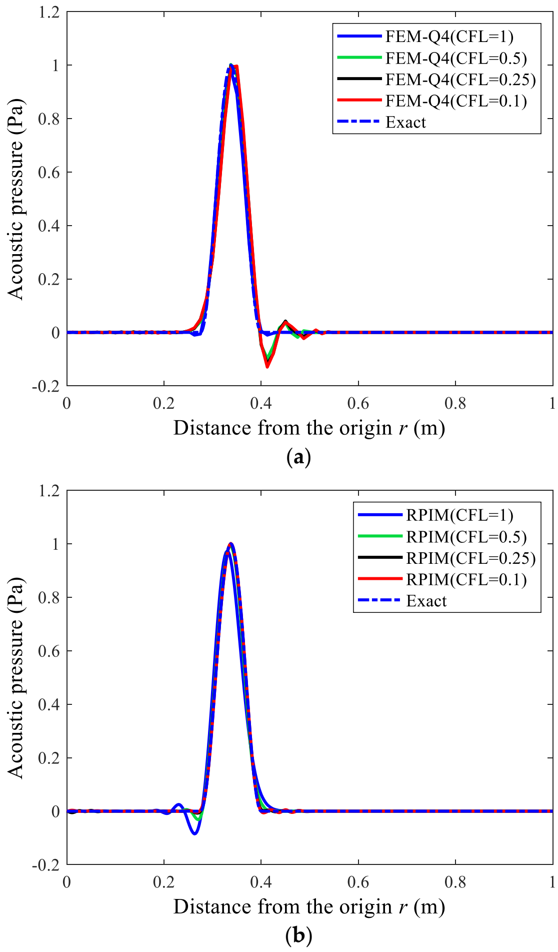

Figure 9. The computed acoustic pressure distribution results from different numerical approaches for the time point t = 0.4 s when the varying non-dimensional time integration steps are employed: (**a**) FEM-Q4; (**b**) RPIM.

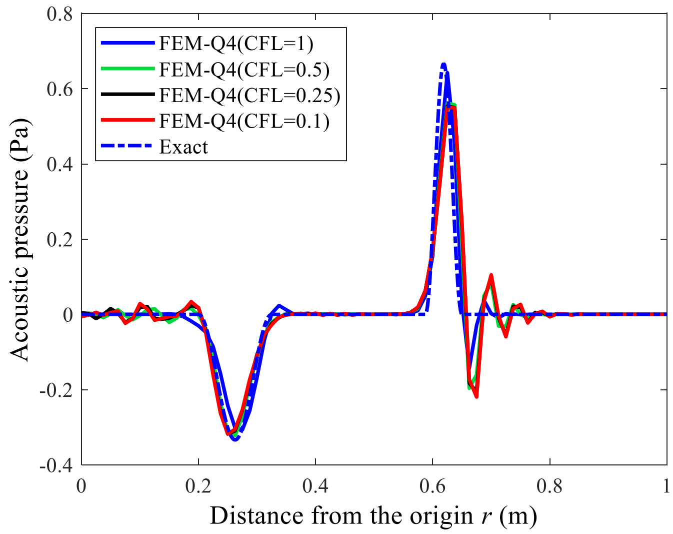

(**a**)

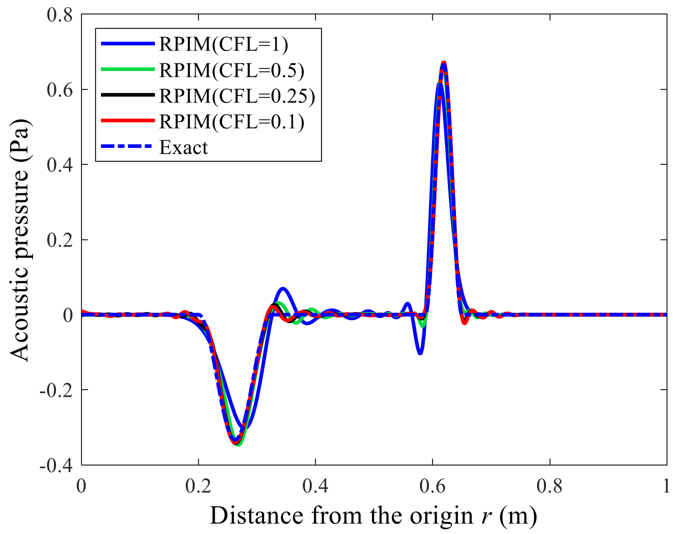

(**b**)

Figure 10. The computed acoustic pressure distribution results from different numerical approaches for the time point t = 0.8 s when the varying non-dimensional time integration steps are employed: (**a**) FEM-Q4; (**b**) RPIM.

Note that the regular node distributions are employed in a previous analysis. This numerical example is further studied by using the irregular node distributions with an average nodal interval of h = 0.0125 m (see Figure 11). Here the employed non-dimensional temporal interval for time integration is CFL = 0.1 m, and the considered time point is t = 0.8 s. The comparisons of the acoustic pressure distribution results for different meshes and different numerical approaches are exhibited in Figure 12. It is quite apparent from these figures that the FEM-Q4 solutions will become worse when the used regular mesh is replaced by the irregular mesh. The main factor for this is that the performance of the traditional FEM-Q4 in numerical analysis is usually sensitive to mesh distortions, and more numerical errors will arise when the distorted mesh patterns are employed. Unlike the traditional FEM-Q4, the present meshfree RPIM shows more powerful abilities in tackling the mesh distortions because the corresponding acoustic pressure distribution results almost cannot be affected when the irregular node distributions are employed for numerical computation. These results may be broadly explained by the fact that the used field function approximation in the meshfree RPIM is usually constructed regardless of the node distributions. This is also one main advantage of the meshfree RPIM compared to the FEM. This numerical feature can further strengthen the abilities of the present meshfree RPIM in transient wave analysis.

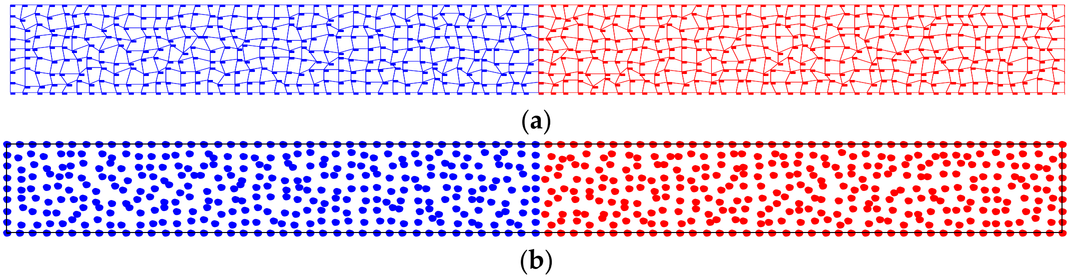

Figure 11. The employed irregular node distributions for the two-dimensional tube: (**a**) FEM-Q4; (**b**) RPIM.

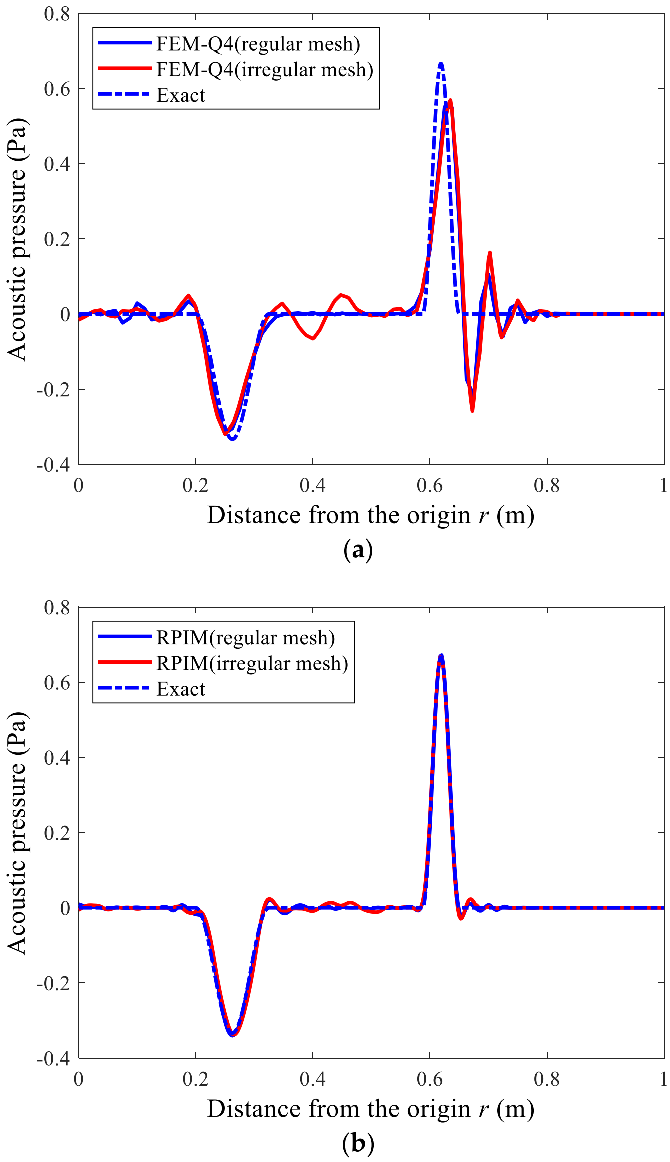

Figure 12. Comparisons of the acoustic pressure distribution results for different meshes and different numerical approaches when the time point $t = 0.8$ s: (**a**) FEM-Q4; (**b**) RPIM.

5.2. The Two-Dimensional Acoustic Wave Scattering Problem by Circular Objects

Another numerical experiment considered here is the two-dimensional acoustic wave scattering problem. Figure 13 displays the geometry configuration of this problem. As shown in Figure 13, several totally identical circular regions are evenly placed in the involved square problem region. The different problem regions are occupied with different acoustic fluid media. The material constants of the involved acoustic fluid media are $\rho_1 = \rho_2$, c_1 = 2 m/s, and c_2 = 1 m/s. The external excitation, $F = 8\pi \sin(20\pi t)$ with $t \in [0, 0.05]$ s, is imposed at the center of the problem domain. In the numerical computation process, only one quadrant problem domain needs to be modeled due to the fact that this transient acoustic wave scattering problem has the symmetry feature (see Figure 13). The standard four-node quadrilateral mesh with an average mesh size of h = 0.01 m is used to perform the required spatial discretization for this numerical experiment. Note that as the exact solution to this problem is not easy to derive, the corresponding numerical solutions from the high-order finite elements using very refined mesh are also provided here as the reference solutions for comparison. In this numerical example, the used non-dimensional time integration step size is measured by CFL = $c_2 \Delta t / h$.

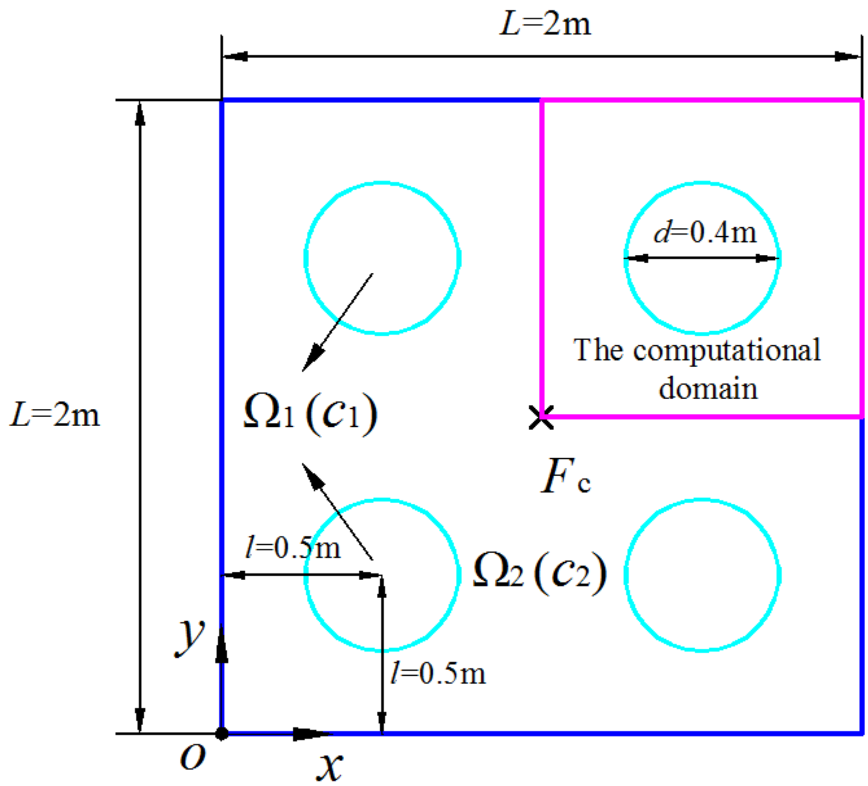

Figure 13. The geometry description of the two-dimensional acoustic wave scattering problem.

For the wave travel angle of $\theta = 45^\circ$ and the non-dimensional time integration size CFL = 0.1, the transient responses of the acoustic pressure distributions at two different time points (t = 0.4 s and t = 0.7 s) are first computed by using different numerical approaches, and the corresponding results are plotted in Figures 14 and 15. In Figure 15, both reflected and transmitted acoustic waves are induced by the interface of different acoustic fluid media; the positions of the interface are also given in Figure 15 using pink lines. The results provided by these figures show that the FEM-Q4 solutions are obviously worse than the meshfree RPIM ones, which match very well with the reference solutions, while the FEM-Q4 solutions obviously deviate quite substantially from the reference solutions. Additionally, the related numerical computations are further performed by considering the different wave travel angles ($\theta = 0^\circ$, $\theta = 22.5^\circ$, and $\theta = 45^\circ$). Figure 16 gives the obtained acoustic pressure distribution results from different numerical approaches.

Figure 16a reveals that the wave travel angle can severely affect the quality of the FEM-Q4 solutions; notably, the numerical anisotropy issue can be clearly observed. While one interesting point that can be seen from Figure 16b is that the above numerical anisotropy issue can be relieved quite substantially by the present meshfree RPIM because the numerical solutions with very similar accuracy can be yielded when the different wave travel angles are considered.

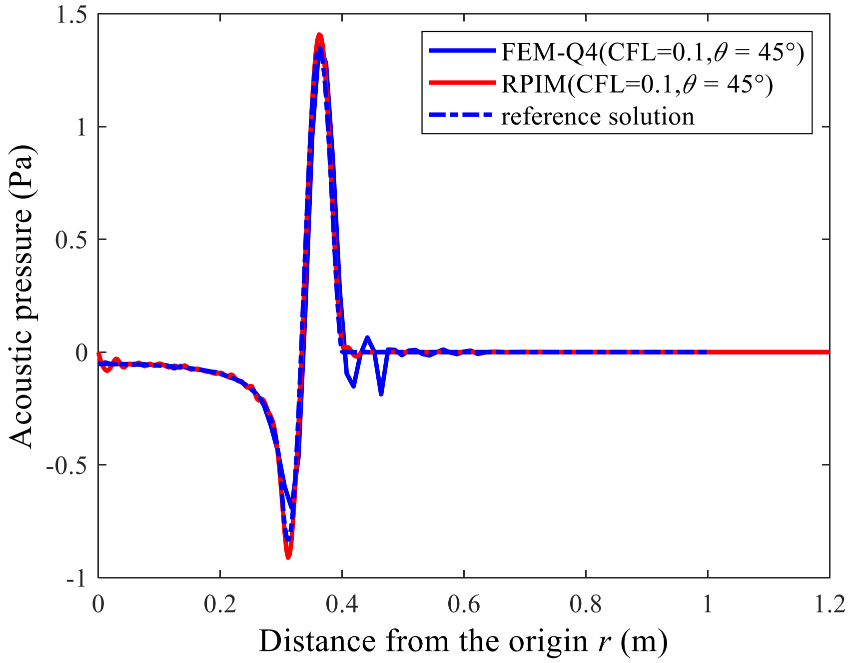

Figure 14. The transient responses of the acoustic pressure distributions from different methods for the two-dimensional scattering problem when the time point $t = 0.4$ s.

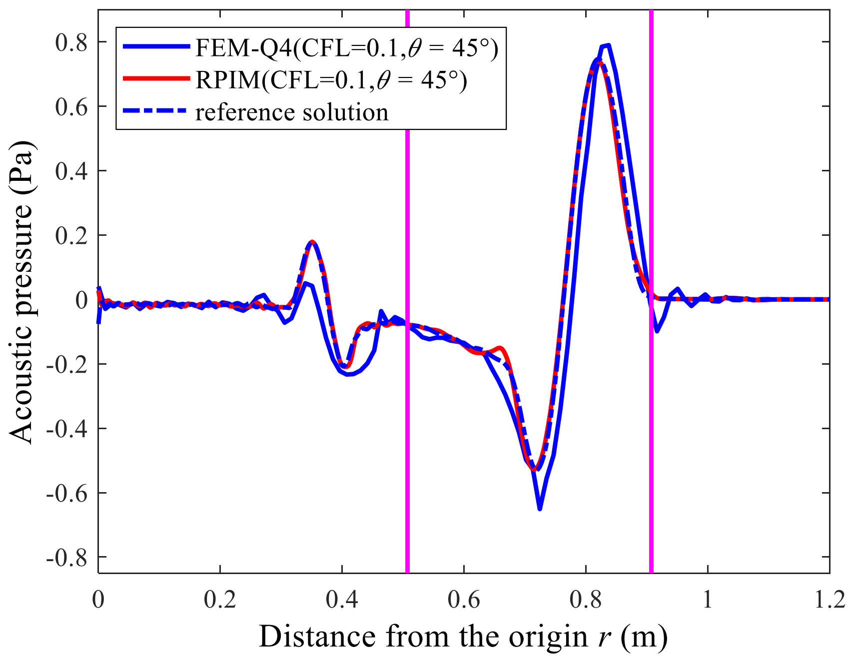

Figure 15. The transient responses of the acoustic pressure distributions from different methods for the two-dimensional scattering problem when the time point $t = 0.7$ s.

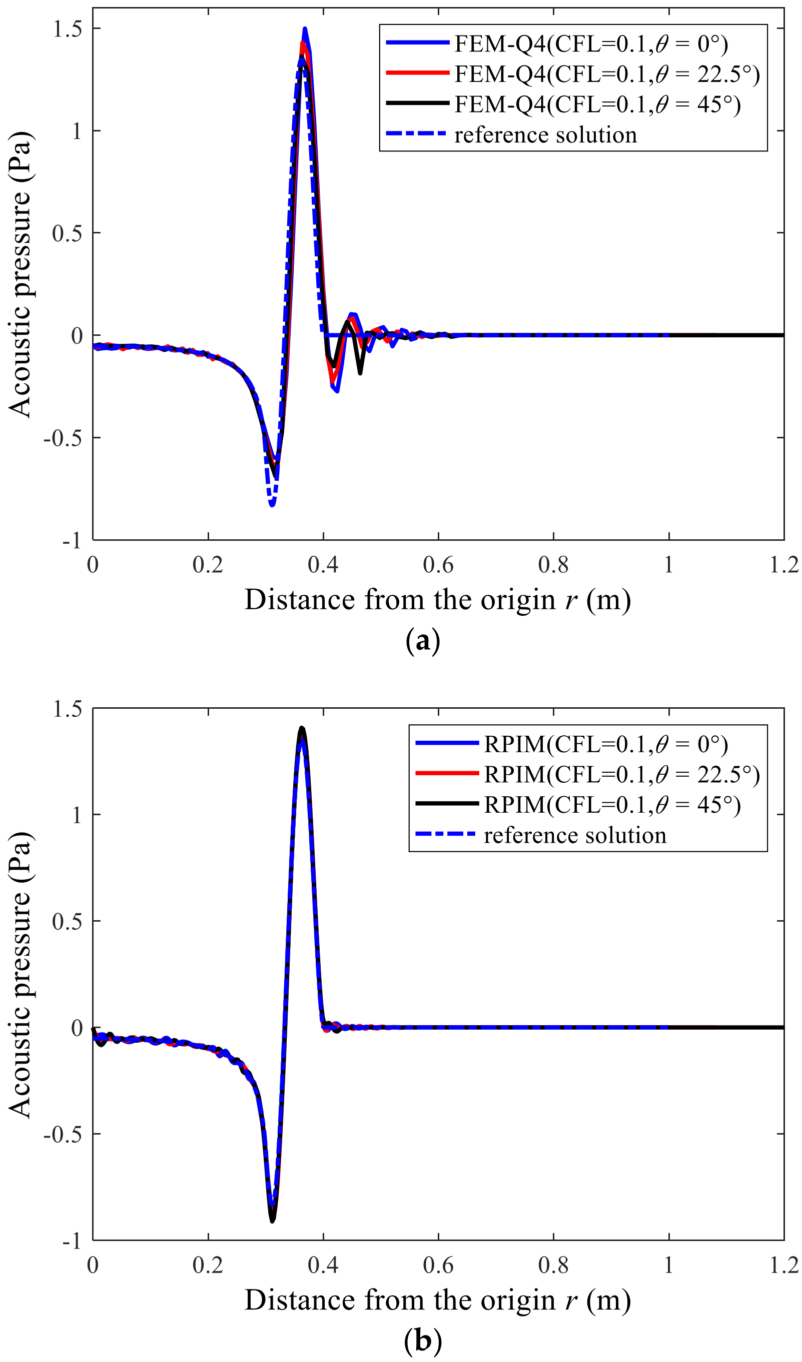

Figure 16. The transient responses of the acoustic pressure distributions from different methods for the two-dimensional scattering problem by considering the different wave travel angles: (**a**) FEM-Q4; (**b**) RPIM.

Next, the varying non-dimensional time integration steps (CFL = 1, CFL = 0.5, CFL = 0.25, and CFL = 0.1) are exploited in the numerical analysis to check whether the monotonic convergence property can be reached in transient wave analysis. For two different time points($t = 0.4$ s and $t = 0.7$ s) and two different angles of wave travel ($\theta = 22.5°$ and $\theta = 45°$), the computed acoustic pressure distributions from different numerical techniques are presented in Figures 17 and 18. The relevant observations from these figures are quite similar to those found in a previous numerical experiment; in particular, the monotonic convergence numerical feature can broadly be reached by the meshfree RPIM and cannot be reached by the conventional FEM-Q4.

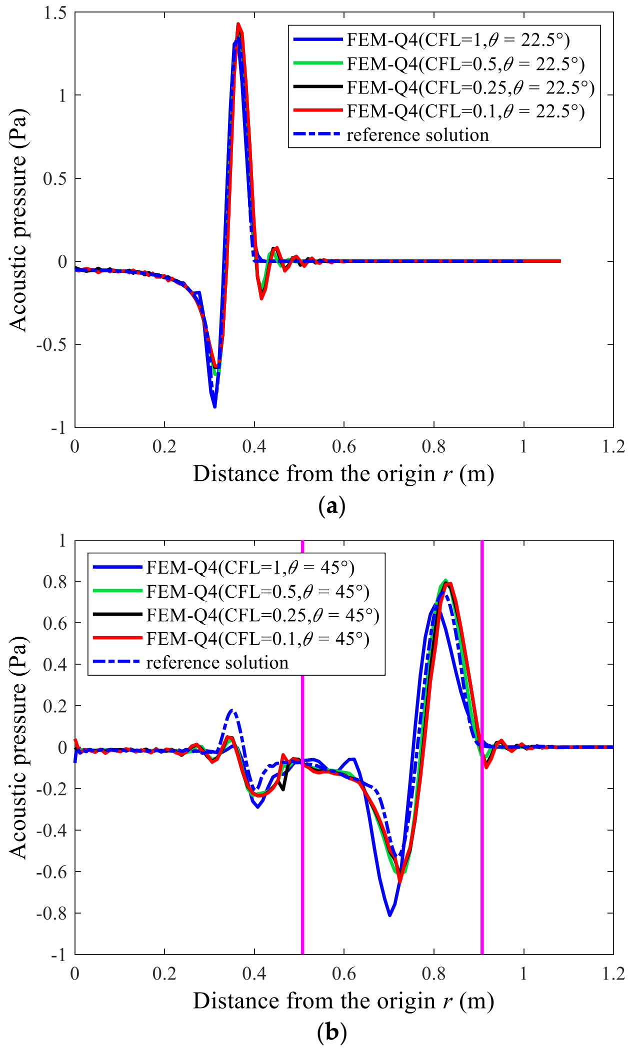

Figure 17. The transient responses of the acoustic pressure distributions at different time points from FEM-Q4 for the two-dimensional scattering problem by using the varying non-dimensional time integration steps: (**a**) $t = 0.4$ s; (**b**) $t = 0.7$ s.

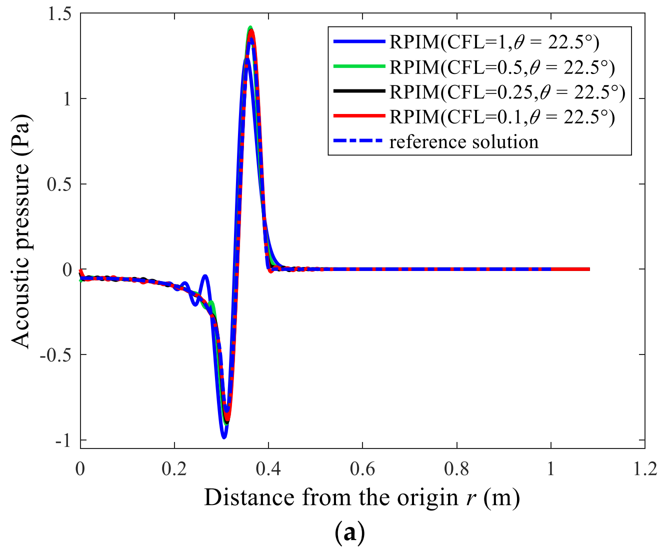

Figure 18. *Cont.*

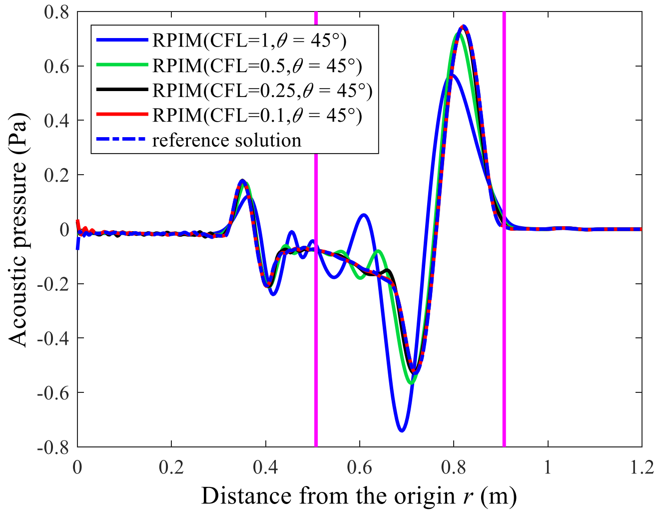

(**b**)

Figure 18. The transient responses of the acoustic pressure distributions at different time points from RPIM for the two-dimensional scattering problem by using the varying non-dimensional time integration steps: (**a**) t = 0.4 s; (**b**) t = 0.7 s.

All of the above numerical solutions suggest that the proposed RPIM with the Bathe time integration method shows stronger abilities and is more suitable for solving transient wave propagations than the conventional FEM-Q4 with totally identical node distributions.

5.3. The Two-Dimensional Acoustic Wave Scattering Problem by Irregular Objects

In the third numerical example, the acoustic wave scattering by irregular objects in two dimensions is considered in testing the numerical performance of the above-mentioned methods in handling irregular problem domains. The details of this numerical experiment are given in Figure 19. The physical constants of acoustic media in different problems are acoustic wave speed c_1 = 2 m/s and c_2 = 1 m/s, acoustic media mass density $\rho_1 = \rho_2$. For this numerical example, the conventional four-node quadrilateral mesh is again employed as the background mesh, and the mean node interval is h = 0.01 m. In this numerical experiment, the employed non-dimensional time interval for time integration is defined as CFL = $c_2\Delta t/h$(Δt is the used time step), and the point excitation at the corner of the problem domain (see Figure 19) is of the following Ricker wavelet form [60]:

$$F = 0.4\left[1 - 2\pi^2 f_p^2 (t - t_s)^2\right] \exp\left(-\pi^2 f_p^2 (t - t_s)^2\right), \tag{27}$$

in which $t_s = 0.1$ s and $f_p = 10$Hz are the defined characteristic parameters.

For the non-dimensional time step CFL = 0.1 and several observation time points (t = 0.7 s, t = 0.8 s, t = 0.9 s and t = 1 s), the computed numerical results of this numerical wave propagation problem in the whole problem domain are displayed in Figures 20 and 21. For comparison purposes, both the standard FEM-Q4 and the present RPIM ($\alpha_h = 3h$) results are furnished here. From the results, it is obvious that considerable numerical errors can be seen in the standard FEM-Q4 solutions. On the contrary, the solutions from the present RPIM are much smoother and show higher computation precision than those from the FEM-Q4. This numerical experiment again demonstrates that the present meshfree RPIM has more excellent numerical performance than the FEM-Q4 in transient wave propagation analysis, even if the irregular problem domains are considered.

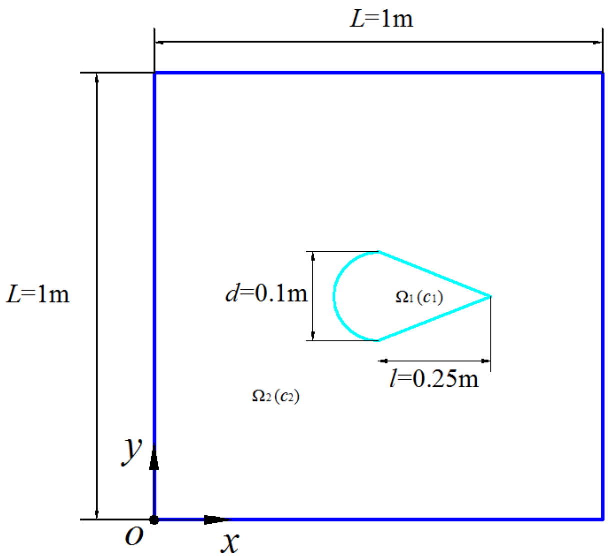

Figure 19. The geometry parameters of the two-dimensional acoustic wave scattering problem by irregular objects.

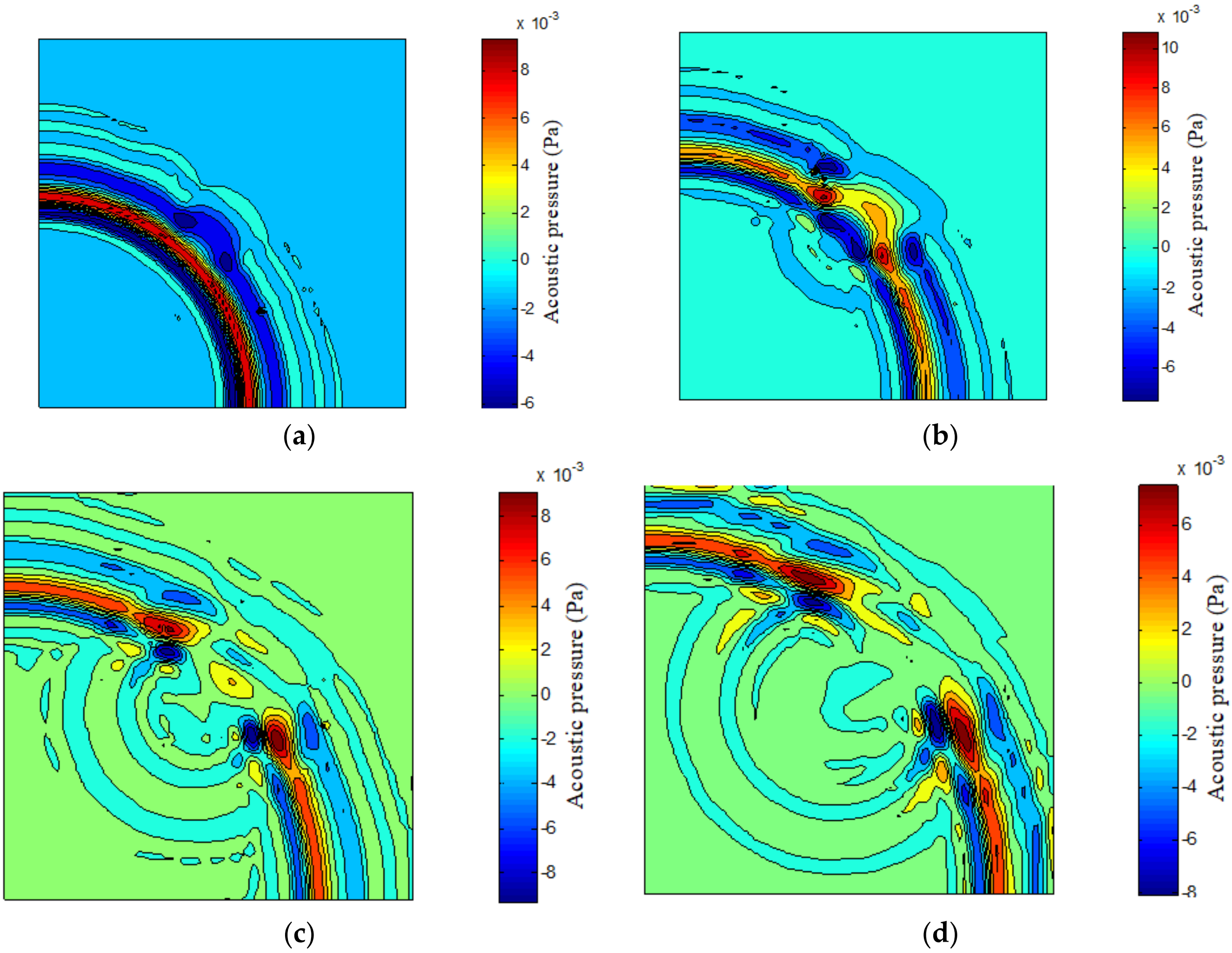

Figure 20. The computed FEM-Q4 results of the acoustic wave scattering by irregular object in the whole problem domain for several observation time points: (**a**) t = 0.7 s; (**b**) t = 0.8 s; (**c**) t = 0.9 s; (**d**) t = 1 s.

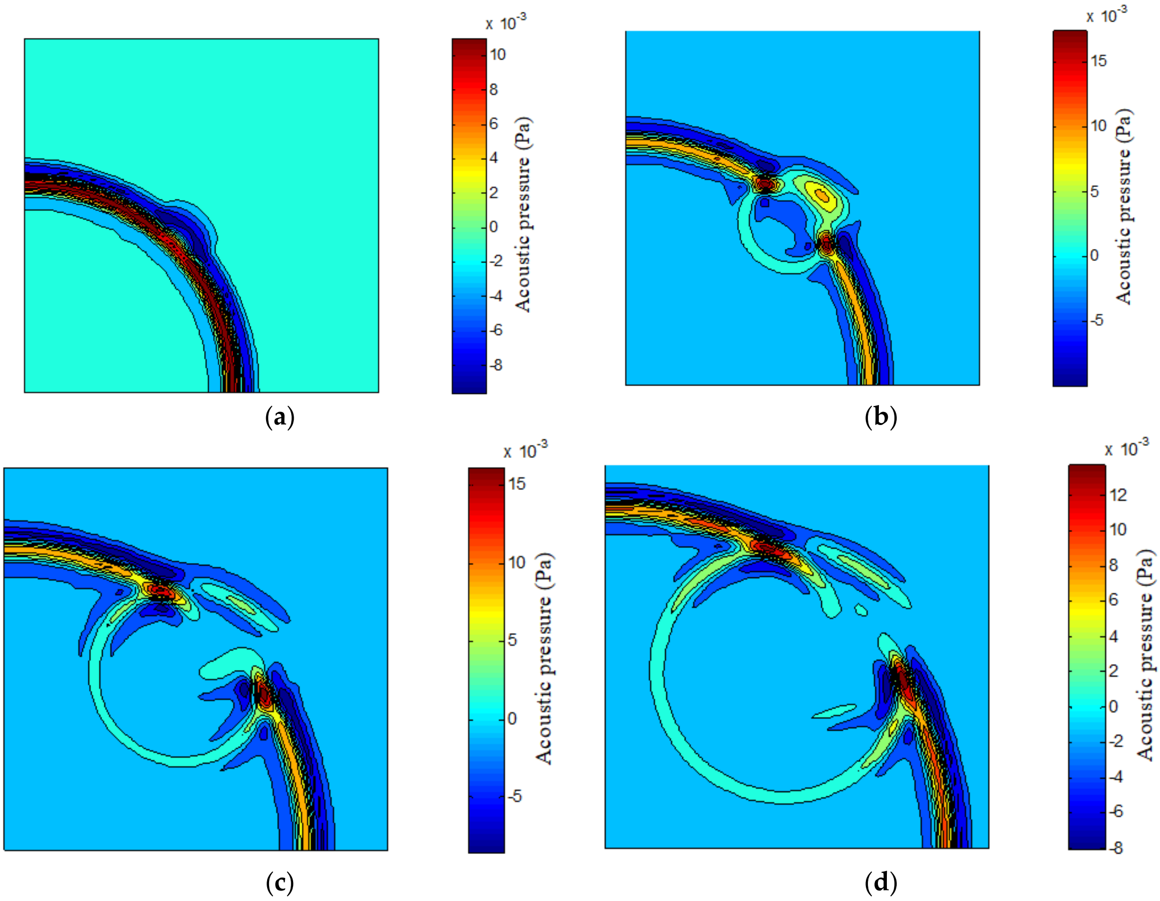

Figure 21. The computed RPIM (α_s = 3 h)results of the acoustic wave scattering by irregular object in the whole problem domain for several observation time points: (**a**) t = 0.7 s; (**b**) t = 0.8 s; (**c**) t = 0.9 s; (**d**) t = 1 s.

5.4. Study on the Computational Cost and Computation Efficiency

In previous numerical analysis, we mainly examine the numerical performance of different spatial discretization techniques (FEM-Q4 and RPIM) in treating the transient wave propagation in non-homogeneous media when the varying non-dimensional time integration step CFL numbers are employed. The important finding is that the present RPIM with adequately large support domains has the valuable monotonic convergence property in transient wave analysis when the Bathe time integration scheme is employed for temporal discretization, while the standard FEM-Q4 does not have this ideal numerical property. Nevertheless, so far, the computational cost and computation efficiency of different spatial discretization methods has not been systemically studied. To examine the abilities of different methods in depth, these issues are studied in this sub-section in great detail. To measure the solution accuracy of the obtained numerical results, the following L^2 relative error norm is employed [70]:

$$e_r = \sqrt{\frac{\int_V (u - u_h)^2 \mathrm{d}V}{\int_V u^2 \mathrm{d}V}}, \tag{28}$$

in which u_h is the numerical solutions, and u represents the corresponding exact solutions or reference solutions.

For the numerical experiments performed in Sections 5.1 and 5.2, the numerical results of computational cost and computational efficiency are detailed and provided in Tables 1 and 2. With the aim to further evaluate the numerical performance of the present meshfree RPIM, the results of another well-developed meshfree technique, which is called the element-free Galerkin method (EFGM), are also given for comparison here. All the involved numerical computation processes are performed in a laptop with a single-core Intel 2.1 GHz CPU and 8Gb RAM. From these two tables, the following valuable remarks can be summarized:

Table 1. The detailed computational cost of different numerical methods in solving the numerical experiment in Section 5.1.

Methods	Number of DOFs	Non-Zero Entities in the System Matrices	CPU Time for Spatial Discretization (s)	Non-Dimensional Time Steps	CPU Time for Temporal Discretization (s)	Total CPU Time (s)	Time Points (s)	Total Numerical Error(%)
FEM-Q4	729	6025	0.78	CFL = 1	3.11	3.89	$t = 0.4$ $t = 0.8$	3.8 14.1
				CFL = 0.5	5.87	6.65	$t = 0.4$ $t = 0.8$	6.04 27.34
				CFL = 0.25	10.09	10.87	$t = 0.4$ $t = 0.8$	8.78 33.89
				CFL = 0.1	14.58	15.36	$t = 0.4$ $t = 0.8$	9.69 36.17
RPIM ($\alpha_s = 3h$)	729	58,029	1.03	CFL = 1	3.56	4.59	$t = 0.4$ $t = 0.8$	5.88 20.14
				CFL = 0.5	6.61	7.64	$t = 0.4$ $t = 0.8$	1.59 7.28
				CFL = 0.25	12.21	13.51	$t = 0.4$ $t = 0.8$	0.89 5.65
				CFL = 0.1	19.09	20.12	$t = 0.4$ $t = 0.8$	0.59 1.58
EFGM ($\alpha_s = 3h$)	729	58,029	1.02	CFL = 1	4.12	5.14	$t = 0.4$ $t = 0.8$	5.13 18.13
				CFL = 0.5	7.23	8.25	$t = 0.4$ $t = 0.8$	1.14 6.17
				CFL = 0.25	13.19	14.21	$t = 0.4$ $t = 0.8$	0.77 4.89
				CFL = 0.1	20.01	21.03	$t = 0.4$ $t = 0.8$	0.37 1.12

(1) For different spatial discretization schemes, the required number of DOFs is totally identical, while the non-zero entities in the obtained system matrices are clearly different. This is because the required number of nodes to assemble the element matrices in the meshfree methods is usually larger than that in the standard FEM.

(2) In performing transient wave propagation analysis, the required total computational time mainly comes from two parts, namely the computing time for spatial discretization and temporal discretization, respectively. Compared to the standard FEM-Q4, more computing time is needed to perform the spatial discretization when the meshfree techniques (RPIM and EFGM) are employed. The reason for this is that in the meshfree approaches, more complex numerical approximation and more expensive numerical integration are always needed.

(3) For all the considered spatial discretization schemes (FEM-Q4, RPIM, and EFGM). The required computing time for temporal discretization is much more than that for spatial discretization. This means that in transient wave propagation analysis, the main required computational cost is from the time integration.

(4) Among the three disparate considered spatial discretization schemes, the standard FEM-Q4 has the highest computational efficiency, while the computation efficiency of the RPIM is the lowest. Though the EFGM is numerically cheaper than the present RPIM, the EFGM always possesses other disadvantages compared to the present RPIM in the numerical process; the related detailed discussion and comparison of RPIM and EFGM can be seen in Ref. [20].

(5) For the RPIM and EFGM, the obtained total relative error can basically become smaller when the smaller non-dimensional time integration step CFL number is employed,

namely the monotonic convergence numerical property can be basically achieved, while the standard FEM-Q4 obviously does not possess this important numerical property.

(6) Although the standard FEM-Q4 is usually numerically cheaper than the meshfree RPIM in solving the transient wave propagation problems, the ideal monotonic convergence property usually can be achieved. This is because the standard FEM-Q4 can always furnish relatively large numerical dispersion errors from the spatial discretization (see Figure 4d). On the contrary, the present RPIM has this ideal numerical property because the meshfree RPIM can generate adequately small spatial discretization errors (see Figure 4c). It is this important numerical property that makes the present RPIM more suitable than the FEM-Q4 in solving the relatively complex transient wave propagation problems (such as wave propagation in non-homogeneous media). This is also the core and main contribution of the present work.

Table 2. The detailed computational cost of different numerical methods in solving the numerical experiment in Section 5.2.

Methods	Number of DOFs	Non-Zero Entities in the System Matrices	CPU Time for Spatial Discretization (s)	Non-Dimensional Time Steps	CPU Time for Temporal Discretization (s)	Total CPU Time (s)	Time Points (s)	Total Numerical Error(%)
FEM-Q4	11,023	97,995	10.89	CFL = 1	54.83	65.72	$t = 0.4$ $t = 0.7$	1.39 10.12
				CFL = 0.5	107.42	118.31	$t = 0.4$ $t = 0.7$	4.09 24.21
				CFL = 0.25	206.83	217.72	$t = 0.4$ $t = 0.7$	7.19 36.84
				CFL = 0.1	419.23	430.12	$t = 0.4$ $t = 0.7$	9.9 46.01
RPIM ($\alpha_s = 3h$)	11,023	1,626,915	17.71	CFL = 1	63.12	80.83	$t = 0.4$ $t = 0.7$	4.12 13.71
				CFL = 0.5	129.53	147.24	$t = 0.4$ $t = 0.7$	3.14 7.63
				CFL = 0.25	264.73	282.44	$t = 0.4$ $t = 0.7$	2.08 3.08
				CFL = 0.1	548.93	466.64	$t = 0.4$ $t = 0.7$	0.51 1.26
EFGM ($\alpha_s = 3h$)	11,023	1,626,915	17.46	CFL = 1	64.18	81.64	$t = 0.4$ $t = 0.7$	3.76 11.23
				CFL = 0.5	132.75	150.21	$t = 0.4$ $t = 0.7$	2.87 6.13
				CFL = 0.25	268.35	285.81	$t = 0.4$ $t = 0.7$	1.64 2.46
				CFL = 0.1	554.27	571.73	$t = 0.4$ $t = 0.7$	0.38 0.76

6. Concluding Remarks

The present work sets out to examine the numerical performance of the meshfree RPIM with the Bathe implicit temporal discretization technique in the transient analysis of wave propagations in non-homogeneous media. The evaluation of the numerical errors is investigated in great detail, and the effects of the required discretizations in the space and time domains on the numerical errors in transient wave analysis are separately analyzed. The results of the dispersion analysis show that the meshfree RPIM has the ability to yield close-to-zero spatial discretization errors as long as the support domain size used for quadrature points is sufficiently large, while this kind of dispersion errors from the standard FEM-Q4 are generally very large. Additionally, it is also shown that the resultant temporal discretization error from the Bathe method is actually a monotonically decreasing function of the non-dimensional time integration steps. Owing to these two factors, the present meshfree RPIM shows distinct advantages over the conventional FEM-Q4 in transient wave analysis.

The strengths of the meshfree RPIM in solving transient wave propagations are confirmed by considering three typical numerical experiments in which the acoustic wave propagations in non-homogeneous media are considered. Since the important monotonic convergence numerical feature with respect to the non-dimensional time integration step can be broadly reached by the present RPIM, the different waves with different travel speeds can be simulated simultaneously with very high computation accuracy. However, the conventional FEM-Q4 generally cannot provide similar numerical solutions. The findings in this research provide further insights into the abilities of different numerical approaches in the analysis of transient wave propagations and also demonstrate that the present meshfree RPIM with the Bathe method can be regarded as a quite competitive alternative to the existing numerical approaches in solving very complex transient wave propagation problems in the practical engineering applications.

Author Contributions: Conceptualization, C.L. and Y.C.; methodology, Y.C.; software, S.M.; validation, C.L. and Y.P.; formal analysis, C.L.; investigation, C.L.; resources, Y.P.; data curation, C.L.; writing—original draft preparation, C.L. and S.M.; writing—review and editing, C.L. and S.M.; visualization, C.L.; supervision, Y.C.; funding acquisition, Y.C. All authors have read and agreed to the published version of the manuscript.

Funding: This research was funded by State Key Laboratory of Ocean Engineering (Shanghai Jiao Tong University) (Grant No. GKZD010081) and the Open Fund of Key Laboratory of High Performance Ship Technology (Wuhan University of Technology), Ministry of Education (Grant No. gxnc21112701).

Institutional Review Board Statement: Not applicable.

Informed Consent Statement: Not applicable.

Data Availability Statement: The data used to support the findings of this study are available from the corresponding author upon request.

Acknowledgments: We thank Zhang for the helpful suggestions to revise the present paper.

Conflicts of Interest: The authors declare no conflict of interest.

References

1. Bathe, K.J. *Finite Element Procedures*, 2nd ed.; Prentice Hall: Watertown, MA, USA, 2014.
2. Li, Y.C.; Dang, S.N.; Li, W.; Chai, Y.B. Free and Forced Vibration Analysis of Two-Dimensional Linear Elastic Solids Using the Finite Element Methods Enriched by Interpolation Cover Functions. *Mathematics* **2022**, *10*, 456. [CrossRef]
3. Noh, G.; Ham, S.; Bathe, K.J. Performance of an implicit time integration scheme in the analysis of wave propagations. *Comput. Struct.* **2013**, *123*, 93–105. [CrossRef]
4. Zheng, Z.Y.; Li, X.L. Theoretical analysis of the generalized finite difference method. *Comput. Math. Appl.* **2022**, *120*, 1–14. [CrossRef]
5. Ju, B.R.; Qu, W.Z. Three-dimensional application of the meshless generalized finite difference method for solving the extended Fisher-Kolmogorov equation. *App. Math. Lett.* **2023**, *136*, 108458. [CrossRef]
6. Qu, W.Z.; He, H. A GFDM with supplementary nodes for thin elastic plate bending analysis under dynamic loading. *Appl. Math. Lett.* **2022**, *124*, 107664. [CrossRef]
7. Fu, Z.J.; Xie, Z.Y.; Ji, S.Y.; Tsai, C.C.; Li, A.L. Meshless generalized finite difference method for water wave interactions with multiple-bottom-seated-cylinder-array structures. *Ocean Eng.* **2020**, *195*, 106736. [CrossRef]
8. Lee, U.; Kim, J.; Leung, A.Y.T. The spectral element method in structural dynamics. *Shock Vib. Dig.* **2000**, *32*, 451–465. [CrossRef]
9. Chai, Y.B.; Gong, Z.X.; Li, W.; Li, T.Y.; Zhang, Q.F. A smoothed finite element method for exterior Helmholtz equation in two dimensions. *Eng. Anal. Bound. Elem.* **2017**, *84*, 237–252. [CrossRef]
10. Chai, Y.B.; Li, W.; Gong, Z.X.; Li, T.Y. Hybrid smoothed finite element method for two-dimensional underwater acoustic scattering problems. *Ocean Eng.* **2016**, *116*, 129–141. [CrossRef]
11. Chai, Y.B.; Li, W.; Gong, Z.X.; Li, T.Y. Hybrid smoothed finite element method for two dimensional acoustic radiation problems. *Appl. Acoust.* **2016**, *103*, 90–101. [CrossRef]
12. Li, W.; You, X.Y.; Chai, Y.B.; Li, T.Y. Edge-Based Smoothed Three-Node Mindlin Plate Element. *J. Eng. Mech.* **2016**, *142*, 04016055. [CrossRef]
13. Li, W.; Gong, Z.X.; Chai, Y.B.; Cheng, C.; Li, T.Y.; Zhang, Q.F.; Wang, M.S. Hybrid gradient smoothing technique with discrete shear gap method for shell structures. *Comput. Math. Appl.* **2017**, *74*, 1826–1855. [CrossRef]
14. Chai, Y.B.; Li, W.; Li, T.Y.; Gong, Z.X.; You, X.Y. Analysis of underwater acoustic scattering problems using stable node-based smoothed finite element method. *Eng. Anal. Bound. Elem.* **2016**, *72*, 27–41. [CrossRef]

15. Chai, Y.B.; Gong, Z.X.; Li, W.; Li, T.Y.; Zhang, Q.F.; Zou, Z.H.; Sun, Y.B. Application of smoothed finite element method to two dimensional exterior problems of acoustic radiation. *Int. J. Comput. Methods* **2018**, *15*, 1850029. [CrossRef]
16. Wang, T.T.; Zhou, G.; Jiang, C.; Shi, F.C.; Tian, X.D.; Gao, G.J. A coupled cell-based smoothed finite element method and discrete phase model for incompressible laminar flow with dilute solid particles. *Eng. Anal. Bound. Elem.* **2022**, *143*, 190–206. [CrossRef]
17. Jiang, C.; Hong, C.; Wang, T.T.; Zhou, G. N-Side cell-based smoothed finite element method for incompressible flow with heat transfer problems. *Eng. Anal. Bound. Elem.* **2023**, *146*, 749–766. [CrossRef]
18. Chai, Y.B.; You, X.Y.; Li, W.; Huang, Y.; Yue, Z.J.; Wang, M.S. Application of the edge-based gradient smoothing technique to acoustic radiation and acoustic scattering from rigid and elastic structures in two dimensions. *Comput. Struct.* **2018**, *203*, 43–58. [CrossRef]
19. Li, W.; Chai, Y.B.; Lei, M.; Li, T.Y. Numerical investigation of the edge-based gradient smoothing technique for exterior Helmholtz equation in two dimensions. *Comput. Struct.* **2017**, *182*, 149–164. [CrossRef]
20. Liu, G.R. *Mesh Free Methods: Moving beyond the Finite Element Method*; CRC Press: Boca Raton, FL, USA, 2009.
21. Chai, Y.B.; You, X.Y.; Li, W. Dispersion Reduction for the Wave Propagation Problems Using a Coupled "FE-Meshfree" Triangular Element. *Int. J. Comput. Methods* **2020**, *17*, 1950071. [CrossRef]
22. You, X.Y.; Li, W.; Chai, Y.B. Dispersion analysis for acoustic problems using the point interpolation method. *Eng. Anal. Bound. Elem.* **2018**, *94*, 79–93. [CrossRef]
23. Lin, J.; Bai, J.; Reutskiy, S.; Lu, J. A novel RBF-based meshless method for solving time-fractional transport equations in 2D and 3D arbitrary domains. *Eng. Comput.* **2022**. [CrossRef]
24. Li, W.; Zhang, Q.; Gui, Q.; Chai, Y.B. A coupled FE-Meshfree triangular element for acoustic radiation problems. *Int. J. Comput. Methods* **2021**, *18*, 2041002. [CrossRef]
25. Wang, C.; Wang, F.J.; Gong, Y.P. Analysis of 2D heat conduction in nonlinear functionally graded materials using a local semi-analytical meshless method. *AIMS Math.* **2021**, *6*, 12599–12618. [CrossRef]
26. Gui, Q.; Zhang, Y.; Chai, Y.B.; You, X.Y.; Li, W. Dispersion error reduction for interior acoustic problems using the radial point interpolation meshless method with plane wave enrichment functions. *Eng. Anal. Bound. Elem.* **2022**, *143*, 428–441. [CrossRef]
27. You, X.Y.; Li, W.; Chai, Y.B. A truly meshfree method for solving acoustic problems using local weak form and radial basis functions. *Appl. Math. Comput.* **2020**, *365*, 124694. [CrossRef]
28. Qu, J.; Dang, S.N.; Li, Y.C.; Chai, Y.B. Analysis of the interior acoustic wave propagation problems using the modified radial point interpolation method (M-RPIM). *Eng. Anal. Bound. Elem.* **2022**, *138*, 339–368. [CrossRef]
29. Liu, G.R.; Gu, Y.T. A meshfree method: Meshfree weak–strong (MWS) form method for 2-D solids. *Comput. Mech.* **2003**, *33*, 2–14. [CrossRef]
30. Cheng, S.; Wang, F.J.; Li, P.W.; Qu, W. Singular boundary method for 2D and 3D acoustic design sensitivity analysis. *Comput. Math. Appl.* **2022**, *119*, 371–386. [CrossRef]
31. Chen, Z.; Sun, L. A boundary meshless method for dynamic coupled thermoelasticity problems. *App. Math. Lett.* **2022**, *134*, 108305. [CrossRef]
32. Cheng, S.F.; Wang, F.J.; Wu, G.Z.; Zhang, C.X. semi-analytical and boundary-type meshless method with adjoint variable formulation for acoustic design sensitivity analysis. *Appl. Math. Lett.* **2022**, *131*, 108068. [CrossRef]
33. Li, J.P.; Zhang, L. High-precision calculation of electromagnetic scattering by the Burton-Miller type regularized method of moments. *Eng. Anal. Bound. Elem.* **2021**, *133*, 177–184. [CrossRef]
34. Li, J.P.; Zhang, L.; Qin, Q.H. A regularized fast multipole method of moments for rapid calculation of three-dimensional time-harmonic electromagnetic scattering from complex targets. *Eng. Anal. Bound. Elem.* **2022**, *142*, 28–38. [CrossRef]
35. Gu, Y.; Fan, C.M.; Fu, Z.J. Localized method of fundamental solutions for three-dimensional elasticity problems: Theory. *Adv. Appl. Math. Mech.* **2021**, *13*, 1520–1534.
36. Li, J.P.; Fu, Z.J.; Gu, Y.; Qin, Q.H. Recent advances and emerging applications of the singular boundary method for large-scale and high-frequency computational acoustics. *Adv. Appl. Math. Mech.* **2022**, *14*, 315–343. [CrossRef]
37. Gu, Y.; Lei, J. Fracture mechanics analysis of two-dimensional cracked thin structures (from micro- to nano-scales) by an efficient boundary element analysis. *Results Math.* **2021**, *11*, 100172. [CrossRef]
38. Fu, Z.J.; Xi, Q.; Gu, Y.; Li, J.P.; Qu, W.Z.; Sun, L.L.; Wei, X.; Wang, F.J.; Lin, J.; Li, W.W.; et al. Singular boundary method: A review and computer implementation aspects. *Eng. Anal. Bound. Elem.* **2023**, *147*, 231–266. [CrossRef]
39. Chen, Z.; Wang, F. Localized Method of Fundamental Solutions for Acoustic Analysis Inside a Car Cavity with Sound-Absorbing Material. *Adv. Appl. Math. Mech.* **2022**, *15*, 182–201. [CrossRef]
40. Wei, X.; Rao, C.; Chen, S.; Luo, W. Numerical simulation of anti-plane wave propagation in heterogeneous media. *App. Math. Lett.* **2023**, *135*, 108436. [CrossRef]
41. Fu, Z.J.; Xi, Q.; Li, Y.; Huang, H.; Rabczuk, T. Hybrid FEM–SBM solver for structural vibration induced underwater acoustic radiation in shallow marine environment. *Comput. Methods Appl. Mech. Eng.* **2020**, *369*, 113236. [CrossRef]
42. Zienkiewicz, O.C. Achievements and some unsolved problems of the finite element method. *Int. J. Numer. Methods Eng.* **2000**, *47*, 9–28. [CrossRef]
43. Monaghan, J.J. Smoothed particle hydrodynamics. *Annu. Rev. Astron. Astrophys.* **1992**, *30*, 543–574. [CrossRef]
44. Liu, W.K.; Jun, S.; Li, S.; Adee, J.; Belytschko, T. Reproducing Kernel particle methods for structural dynamics. *Int. J. Numer. Methods Eng.* **1995**, *38*, 1655–1679. [CrossRef]

45. Belytschko, T.; Lu, Y.Y.; Gu, L. Element-free Galerkin methods. *Int. J. Numer. Methods Eng.* **1994**, *37*, 229–256. [CrossRef]
46. Li, X.; Li, S. A fast element-free Galerkin method for the fractional diffusion-wave equation. *App. Math. Lett.* **2021**, *122*, 107529. [CrossRef]
47. Li, X.; Li, S. A linearized element-free Galerkin method for the complex Ginzburg–Landau equation. *Comput. Math. Appl.* **2021**, *90*, 135–147. [CrossRef]
48. Lai, B.; Bathe, K.J. The method of finite spheres in three-dimensional linear static analysis. *Comput. Struct.* **2016**, *173*, 161–173. [CrossRef]
49. Li, X.; Li, S. A finite point method for the fractional cable equation using meshless smoothed gradients. *Eng. Anal. Bound. Elem.* **2022**, *134*, 453–465. [CrossRef]
50. Fu, Z.J.; Tang, Z.C.; Xi, Q.; Liu, Q.G.; Gu, Y.; Wang, F.J. Localized collocation schemes and their applications. *Acta Mech. Sinica* **2022**, *38*, 422167. [CrossRef]
51. Fu, Z.J.; Yang, L.W.; Xi, Q.; Liu, C.S. A boundary collocation method for anomalous heat conduction analysis in functionally graded materials. *Comput. Math. Appl.* **2021**, *88*, 91–109. [CrossRef]
52. Tang, Z.; Fu, Z.J.; Sun, H.; Liu, X. An efficient localized collocation solver for anomalous diffusion on surfaces. *Fract. Calc. Appl. Anal.* **2021**, *24*, 865–894. [CrossRef]
53. Xi, Q.; Fu, Z.J.; Rabczuk, T.; Yin, D. A localized collocation scheme with fundamental solutions for long-time anomalous heat conduction analysis in functionally graded materials. *Int. J. Heat Mass Tran.* **2021**, *180*, 121778. [CrossRef]
54. Noh, G.; Bathe, K.J. An explicit time integration scheme for the analysis of wave propagations. *Comput. Struct.* **2013**, *129*, 178–193. [CrossRef]
55. Kim, W.; Reddy, J.N. Novel explicit time integration schemes for efficient transient analyses of structural problems. *Int. J. Mech. Sci.* **2000**, *172*, 105429. [CrossRef]
56. Noh, G.; Bathe, K.J. Further insights into an implicit time integration scheme for structural dynamics. *Comput. Struct.* **2018**, *202*, 15–24. [CrossRef]
57. Song, C.M.; Eisenträger, S.; Zhang, X.R. High-order implicit time integration scheme based on Padé expansions. *Comput. Methods Appl. Mech. Eng.* **2022**, *390*, 114436. [CrossRef]
58. Bathe, K.J. Conserving energy and momentum in nonlinear dynamics: A simple implicit time integration scheme. *Comput. Struct.* **2007**, *85*, 437–445. [CrossRef]
59. Zhang, Y.O.; Dang, S.N.; Li, W.; Chai, Y.B. Performance of the radial point interpolation method (RPIM) with implicit time integration scheme for transient wave propagation dynamics. *Comput. Math. Appl.* **2022**, *114*, 95–111. [CrossRef]
60. Chai, Y.B.; Bathe, K.J. Transient wave propagation in inhomogeneous media with enriched overlapping triangular elements. *Comput. Struct.* **2020**, *237*, 106273. [CrossRef]
61. Chai, Y.B.; Li, W.; Liu, Z.Y. Analysis of transient wave propagation dynamics using the enriched finite element method with interpolation cover functions. *Appl. Math. Comput.* **2022**, *412*, 126564. [CrossRef]
62. Sun, T.T.; Wang, P.; Zhang, G.J.; Chai, Y.B. Transient analyses of wave propagations in nonhomogeneous media employing the novel finite element method with the appropriate enrichment function. *Comput. Math. Appl.* **2023**, *129*, 90–112. [CrossRef]
63. Fasshauer, G.E.; Zhang, J.G. On choosing "optimal" shape parameters for RBF approximation. *Numer. Algorithms* **2007**, *45*, 345–368. [CrossRef]
64. Liu, G.R.; Gu, Y.T. Assessment and applications of point interpolation methods for computational mechanics. *Int. J. Numer. Meth. Eng.* **2004**, *59*, 1373–1397. [CrossRef]
65. Liu, G.R.; Gu, Y.T. *An Introduction to Meshfree Methods and Their Programming*; Springer Science & Business Media: Dordrecht, The Netherlands, 2005.
66. Li, Y.C.; Liu, C.; Li, W.; Chai, Y.B. Numerical investigation of the element-free Galerkin method (EFGM) with appropriate temporal discretization techniques for transient wave propagation problems. *Appl. Math. Comput.* **2023**, *442*, 127755. [CrossRef]
67. Wu, F.; Zhou, G.; Gu, Q.Y.; Chai, Y.B. An enriched finite element method with interpolation cover functions for acoustic analysis in high frequencies. *Eng. Anal. Bound. Elem.* **2021**, *129*, 67–81. [CrossRef]
68. Gui, Q.; Zhou, Y.; Li, W.; Chai, Y.B. Analysis of two-dimensional acoustic radiation problems using the finite element with cover functions. *Appl. Acoust.* **2022**, *185*, 108408. [CrossRef]
69. Chai, Y.B.; Gong, Z.X.; Li, W.; Zhang, Y.O. Analysis of transient wave propagation in inhomogeneous media using edge-based gradient smoothing technique and bathe time integration method. *Eng. Anal. Bound. Elem.* **2020**, *120*, 211–222. [CrossRef]
70. Kim, K.T.; Zhang, L.; Bathe, K.J. Transient implicit wave propagation dynamics with overlapping finite Elements. *Comput. Struct.* **2018**, *199*, 18–33. [CrossRef]